Master's Thesis

A Study on the Flow Characteristics and Primary Energy Conversion in a Direct Drive Turbine for Wave Power Generation

Supervisor: Prof. Dr. Young-Ho LEE

July 2010

Department of Mechanical Engineering
Graduate School of Korea Maritime University

Deepak Divashkar Prasad

We certify that we have read this thesis and that, in our opinion, it is satisfactory in scope and quality as a thesis for the degree of Master of Mechanical Engineering, submitted by Deepak Divashkar Prasad.

THESIS COMMITTEE

Chairperson: Prof. Dr. You-Taek KIM
Marine System Engineering, Korea Maritime University

Co-Chairperson: Prof. Dr. Kweon-Ha PARK
Division of Mechanical & Information Engineering, Korea Maritime University

Supervisor: Prof. Dr. Young-Ho LEE
Division of Mechanical & Information Engineering, Korea Maritime University

July 2010

Department of Mechanical Engineering
Graduate School of Korea Maritime University

본 論文을 디팍 디바스칼 프라사드의 工學碩士
學位論文으로 認准함

위원장: 공학박사 김 유 택 (인)

위 원: 공학박사 박 권 하 (인)

위 원: 공학박사 이 영 호 (인)

July 2010

한국해양대학교 대학원

기 계 공 학 과

Table of Content

A Study on the Flow Characteristics and Primary Energy Conversion in a Direct Drive Turbine for Wave Power Generation

Deepak Divashkar Prasad

Department of Mechanical Engineering
Graduate School of Korea Maritime University

Abstract

Due to recent developments such as increasing price of fossil fuels and environmental issues associated with fossil fuels, there is a need to find alternative energy supplies. Wave energy offers such a solution. Wave energy is the most consistent of all the intermittent renewable energy sources. In addition to this, very large energy fluxes occur in the ocean waves and by using appropriate wave energy converters the energy can be harnessed. The present study looks at utilizing a direct drive turbine of cross flow type to extract energy from the incoming waves. Currently, the model does not include the runner. The purpose of the present study is stated below:

- Successfully simulating waves in a numerical wave tank (NWT) using the commercial code of ANSYS CFX.
- Study flow characteristics in the front guide nozzle, augmentation channel and the rear chamber of the base model. Obtain water power and primary energy conversion for the base model.
- Conduct simulation of the entire model at different wave period to obtain the best wave condition to achieve maximum water power.
- Maximize the primary energy conversion of the base model by making modifications to front guide nozzle, augmentation channel and the rear chamber.

After obtaining the best designs of all the individual components, that is the front guide nozzle, augmentation channel and the rear chamber; a final model was obtained and its performance with respect to the base mode was investigated. The water power and the primary energy conversion for the base model was 29.9W and 0.5 respectively. On the other hand, for the final model the water power and the primary energy conversion were 40.2W and 0.67 respectively. This represents an increase of 34% in primary energy conversion when compared to the base model.

In addition to this, the overall optimization yields better flow characteristics in the front guide nozzle, the augmentation channel and in the rear chamber of the final model. Average velocity in the front guide nozzle of the final model is 16% higher than the base model and also an increase of 10% is recorded for the peripheral velocity. This improvement thus leads to higher energy conversion.

Nomenclature

A_{CS} : cross sectional area	[m^2]
C_f : first stage energy conversion factor	[-]
c_g : group velocity	[m/s]
c_p : phase velocity	[m/s]
d : water depth	[m]
E : energy density	[J/m^2]
E_A : entrance arc	[°]
g : acceleration due to gravity	[m^2/s]
H : wave height	[m]
H_{0i} : cross sectional height at section i	Im]
$\triangle H$: head difference	[m]
L_0 : front guide nozzle length	[m]
P_{Avail} : available power at front guide nozzle inlet	[W]
P_{WP} : water power	[W]
P_{Wave} : wave energy flux	[W/m]
Q : volume flow rate	[m^3/s]
R_L : lower corner fillet	[mm]
R_U : upper corner fillet	[mm]

T : wave period [s]

V : volume [m^3]

v_t : mean velocity in the numerical wave tank [m/s]

W_G : front guide nozzle inlet width [m]

W_{0i} : cross sectional width at section i [m]

$\triangle Y$: rear chamber water level difference [m]

α : front guide nozzle divergence angle [°]

λ : wavelength [m]

ρ : water density [kg/m^3]

CHAPTER 1 INTRODUCTION

1.1 Background

Utilization of renewable energy supplies is inevitable as fossil fuels become increasingly expensive and are depleting at a remarkable rate as the demand for quality energy supply increases with an increase in the world's population. In addition to this, it is the countermeasure against environmental issues, for example pollution and global warming.

Renewable energy is the energy obtained from the continuous or repetitive currents of energy occurring in the natural environment for instance solar energy and wind energy. For this reason, renewable energy sources are fundamentally different from fossil fuels, and do not produce as many greenhouse gases and other pollutants as fossil fuel combustion [1]. The energy is passing through the environment as a current or flow, irrespective of there being a manmade device to intercept and harness this power. Path ABC in Fig. 1.1 shows the environmental energy flow and path DEF shows the harnessed energy flow Renewable energy flows involve natural phenomena such as sunlight, wind, tides and geothermal heat. Each of these sources has unique characteristics which influence how and where they are used.

The majority of renewable energy technologies are directly or indirectly powered by the Sun. as shown in Fig. 1.2. The hydrosphere (water) absorbs a major fraction of the incoming radiation. Most radiation is absorbed at low latitudes around the equator, but this energy is dissipated around the globe in the form of winds and ocean currents. Wave motion may play a role in the process of transferring mechanical energy between the atmosphere and the ocean through wind stress. Solar energy is also responsible for the distribution of precipitation which is tapped by hydroelectric projects, and for the growth of plants used to create biofuels.

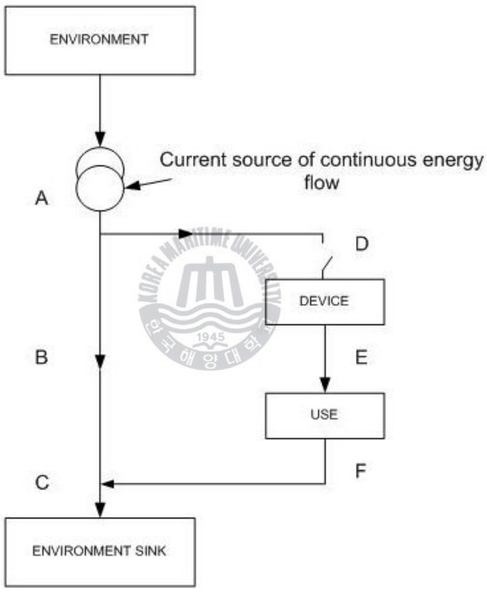

Figure 1.1 Renewable Energy System [1]

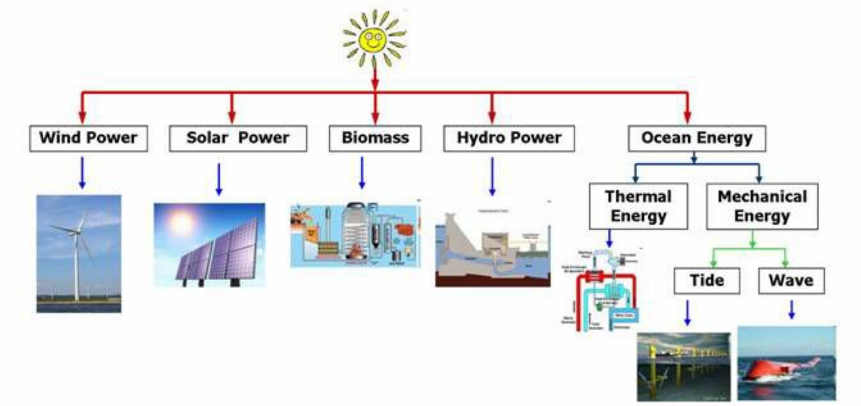

Figure 1.2 Renewable Energy Resources

The ocean contains vast amount of energy in form of thermal energy and mechanical energy. Mechanical energy can further by divided into tides and waves. However, the present study deals with wave energy conversion. The global power potential represented by waves that hit all the coasts worldwide has been estimated to be in the order of 1 TW [2]. On an average, each wave crest transmits 10-50 kW/m of energy and this corresponds to 15 to 20 times more energy per meter than wind or solar [3]. As most forms of renewable sources, wave energy is unevenly distributed over the globe. An increased wave activity is found between the latitudes 30° and 60° on both side of the hemisphere as shown in Fig. 1.3. In general, the waves present on the western edge of the continents contain more energy because of the prevailing west to east winds [4].

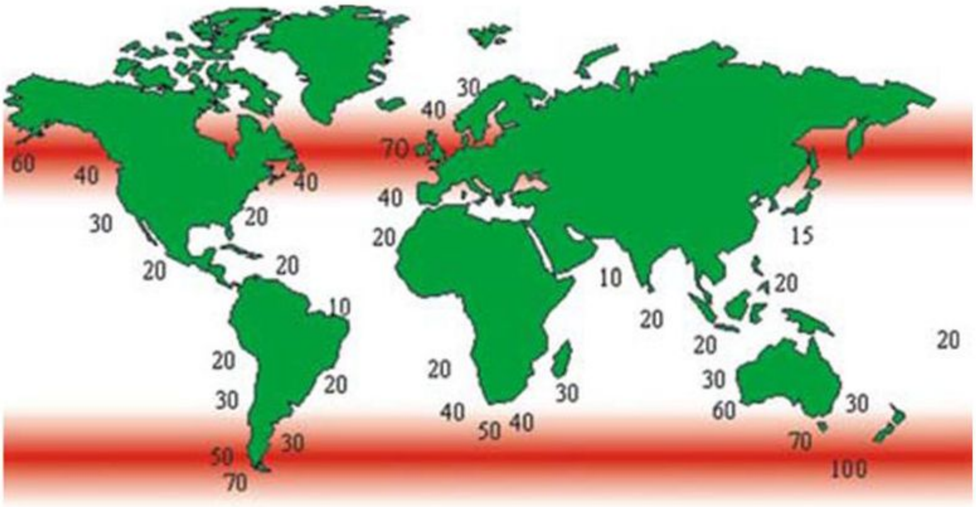

Figure 1.3 Approximate Global Distribution of Wave Power Levels in kW/m of Wave Front [5]

Ocean surface waves are mechanical waves that propagate along the interface between water and air; the restoring force is provided by gravity, and so they are often referred to as surface gravity waves. As the wind blows, pressure and friction forces perturb the equilibrium of the ocean surface. These forces transfer energy from the air to the water, forming waves. Figure 1.4 shows the formation of ocean surface waves.

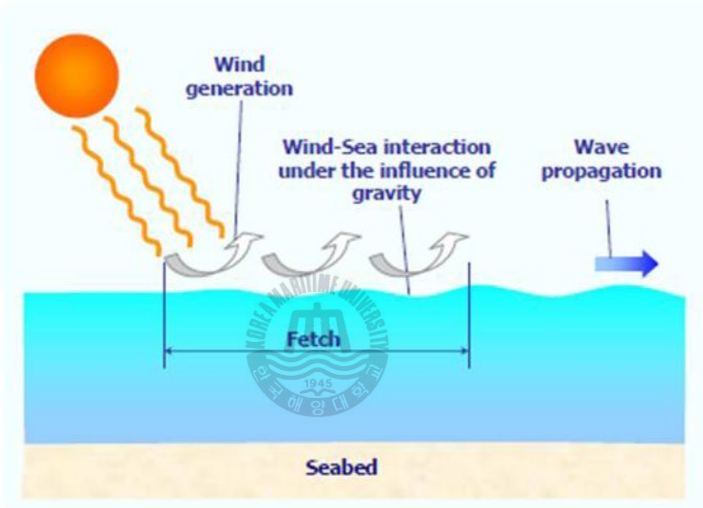

Figure 1.4 Ocean Surface Wave Formation [6]

Ocean waves encompass two forms of energy; kinetic energy and potential energy. Kinetic energy is due to the motion of the particles and potential energy due to the vertical elevation of the water from the mean sea level. On the average, the kinetic energy in a wave is equal to the potential energy [7]. The power in the wave is proportional to the square of wave height and to the period of the motion.

In the case of monochromatic linear plane waves in deep water (where the depth is more than half the wavelength, (d > λ/2), particles near the surface move in circular paths, making ocean surface waves a combination of longitudinal (back and forth) and transverse (up and down) wave motions. When waves propagate in shallow water, (where the depth is less than 0.05 the wavelength, d < λ/20) the particle trajectories are compressed into ellipses. As the wave amplitude increases, the particle paths no longer form closed orbits; rather, after the passage of each crest, particles are displaced a little forward from their previous positions, a phenomenon known as Stokes drift. In shallower waters, water movement occurs against the sea bottom which leads to energy dissipation. Waves that propagate in depths between shallow and deep water, (λ/20 < d > λ/2) are called intermediate depth waves. Deep water wave and shallow water wave propagation is shown in Fig. 1.5.

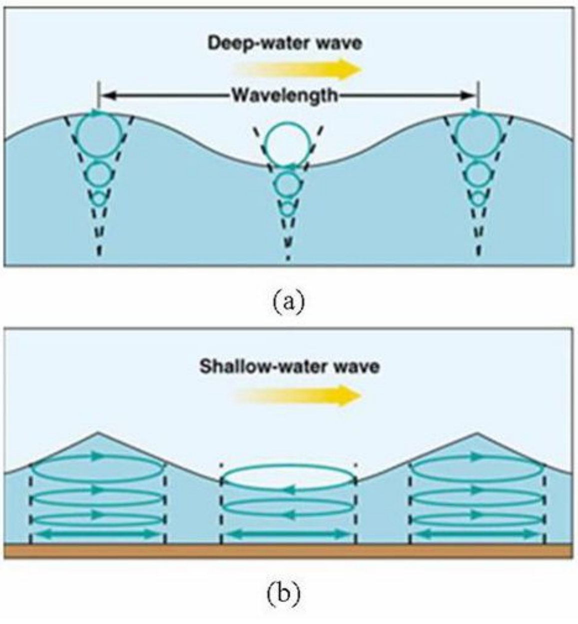

Figure 1.5 Orbital Motion in Deep Water Waves (a) and Shallow Water Waves (b) [8]

Wave energy is:

- truly renewable - inexhaustible and occurring from natural phenomenon.
- the most consistent of the intermittent renewable energy sources.
- non-emitting - no emissions of harmful pollutants result from its use.
- consumes no fuel in the operation of the system

Intermittent sources are those that operate only when the resource is available. While wind, solar and wave are all intermittent, wave is the most consistent. Wind does not blow constantly and the absolute amount of wind in any one area is highly variable and dependent on ground level. Solar availability varies with location, time of day and season. Waves, however, remain throughout the day even though wave swells do change in power and size. Availability of waves is 90% compared to 30% availability of wind and solar energy.

The distinctive advantage of wave power is the large energy fluxes available and the predictability of wave conditions over a certain time span. The power flow in waves is approximately five times more than the wind that generates the waves; this makes wave energy more persistent than wind energy [9].

1.2 Wave Energy Converters

The many advantageous associated with wave energy as highlighted in the previous section makes it a suitable energy source to harness to meet the increasing energy demands and at the same time it is environmentally friendly. Inventors for more than two centuries have proposed many different devices or utilizing wave power for human purpose such as electricity generation, desalination and pumping of water in reservoirs [10-17].

Japanese wave-power pioneer Yoshio Masuda [18] in late 1940s started to test and develop wave-energy devices. Stephen Salter [19-20] and Kjell Budal [21] initiated in 1973 wave-power research at universities in Scotland and Norway, respectively. In the US, Michael E. McCormick [22] was an early academic wave power researcher. In years following the oil crisis in 1973, many researchers at universities and other institutions took up the subject of wave energy. During the early 1980s, when the petroleum price declined, wave-energy funding was drastically reduced [23]. A few first generation prototypes were, nevertheless, tested in the sea but following the Kyoto protocol on reduction of CO_2 emission to the atmosphere, there is again a growing interest for wave-energy research and development in many countries.

Wave energy conversion devices have stimulated the imagination of designers and given birth to a lot of different concepts. Wave power devices are generally categorized by the method used to capture the energy of the waves. They can also be categorized by location and power take-off system.

- **Method types** are point absorber or buoy; surfacing following or attenuator; terminator, lining perpendicular to wave propagation; oscillating water column; and overtopping.

- **Locations** are shoreline, nearshore and offshore.
- **Types of power take-off** include: hydraulic ram, elastomeric hose pump, pump-to-shore, hydroelectric turbine, air turbine, and linear electrical generator. Some of these designs incorporate parabolic reflectors as a means of increasing the wave energy at the point of capture.

Few of the best known device concepts are listed below:

- Point absorbers
- Oscillating Water Columns (OWC)
- Overtopping terminators
- Attenuator

Point absorber – Utilizes wave energy from all directions at a single point by using the vertical motion of waves [24]. The length (along the direction of wave propagation) and width of a point absorber are small compared to the usual wave length. The majority of wave energy converter designs are point absorbers. They can be either floating or submerged devices.

One of the floating device configurations is called a hose pump point absorber. It consists of a surface-floating buoy anchored to the sea bed, with the turbine device as part of the vertical connection. Energy transfer takes place by converting the vertical component of wave kinetic energy into pressurized seawater by means of two-stroke hose pumps. The pressurized seawater is directed into an energy conversion system consisting of a turbine driving an electrical generator. Example of this configuration is the AquaBuoy by Finavera Renewables Inc. [25] which is shown in Fig. 1.6.

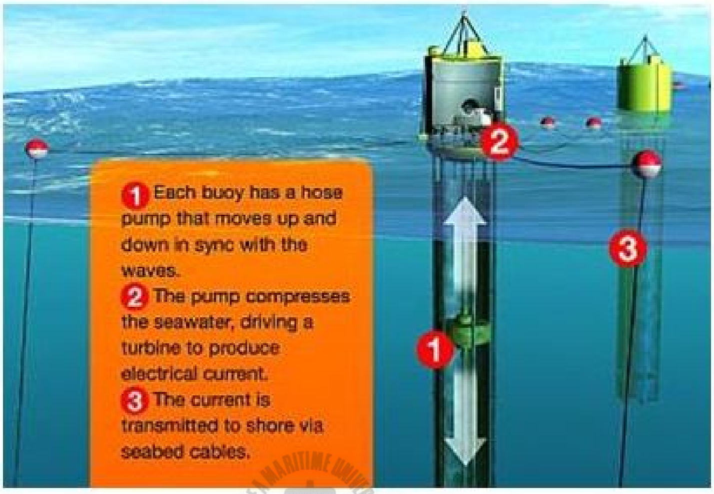

Figure 1.6 Floating Type Point Absorber (AquaBuoy) [26]

A good example of a submerged point absorber is the Archimedes Wave Swing (AWS) [27-28] which generates electricity by drawing energy from sea swells. The AWS consists of two cylinders. The lower cylinder is fixed to the sea floor while the upper cylinder moves up and down under the influence of waves as shown in Fig. 1.7. Simultaneously, magnets, which are fixed to the upper cylinder, move along a coil. As a result, the motion of the floater is damped and electricity is produced. The interior of the AWS is filled with air and when the upper cylinder moves downwards, the air inside is pressurized. As a result, a counteracting force is created which forces the upper cylinder to move up again.

As a wave crest approaches, the water pressure on the top of the cylinder increases and the upper part or 'floater' compresses the gas within the cylinder to balance the pressures. The reverse happens as the wave trough passes and the cylinder expands. The relative movement between the floater and the lower part or silo is converted to electricity by means of a hydraulic system and motor-generator set.

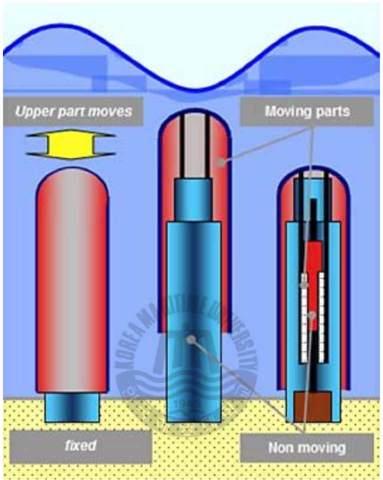

Figure 1.7 Submerged Type Point Absorber
(Archimedes Wave Swig) [28]

Oscillating Water Column (OWC) - is a partially-submerged, hollow structure positioned, either vertically or at an angle, either in shallow water or onshore. OWC uses the same principle as a piston in an engine [29]. It generates electricity in a two step process. As a wave enters the column, the entrained air which is held over the column of water is forced past a turbine and increases the pressure within the column. As the wave retreats, the air is drawn back past the turbine due to the reduced air pressure on the ocean side of the turbine. Most commonly a Wells turbine is used in OWC because it has the advantage of rotating in the same direction irrespective of the airflow direction.

OWC can be either onshore or nearshore or offshore. Onshore OWC is relatively cheap because there is no need for sub sea grid connection, easier to maintain and has easy accessibility. However, onshore OWC devices capture less wave energy due to seabed friction when compared to there nearshore and offshore counterparts. An example of onshore OWC as shown in Fig. 1.8 is the LIMPET (Land Installed Marine Powered Energy Transformer) on Island of Islay in Scotland constructed by WAVEGEN [30].

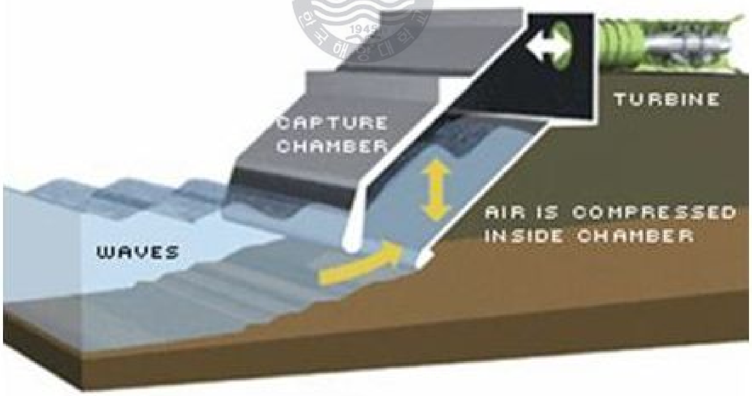

Figure 1.8 Cut Away View of the LIMPET [31]

The Mighty Whale [32] developed by JAMSTEC (Japanese Agency for Marine-Earth Science and Technology) is an example of offshore OWC. The prototype is moored to face the predominant wave direction as shown in Fig. 1.9. It contains three air chambers that convert wave energy into pneumatic energy. Wave action causes the internal water level in each chamber to rise and fall, forcing a bi-directional airflow over an air turbine.

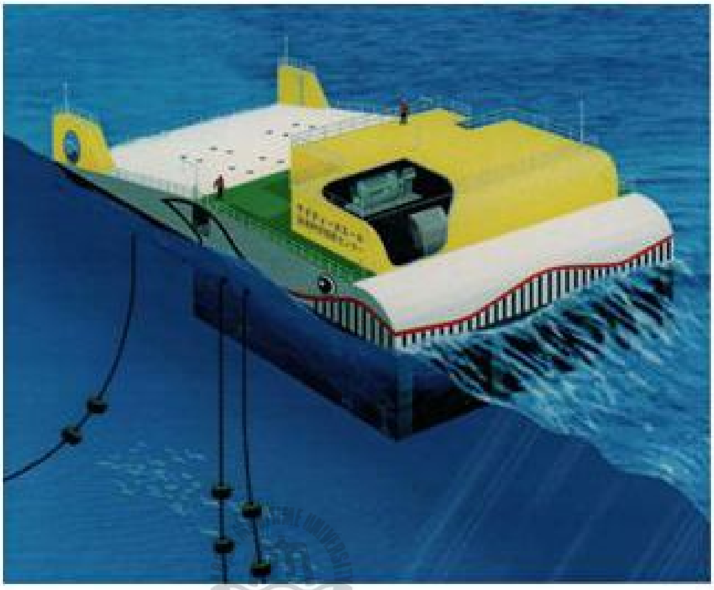

Figure 1.9 Mighty Whale an Example of Offshore OWC [32]

Overtopping terminators - Wave energy devices oriented perpendicular to the direction of the wave, are known as terminators. In overtopping terminators, the wave is first concentrated by wings and then focused towards a central reservoir. The amplified waves surge up a ramp and fills a reservoir at a level above sealevel. The potential energy of the water trapped in the reservoir is then converted to electrical energy through a low head turbine which is connected to a generator. Perhaps the best known overtopping device today is the Wave Dragon [33] as shown in Fig.1.10, made by a Danish company, Wave Dragon ApS. In order to use waves to push water up to a higher level, a principle called tapered channeling

(TAPCHAN) is used. The two wings of the Wave Dragon are used to focus the waves towards a narrow gap or focus point.

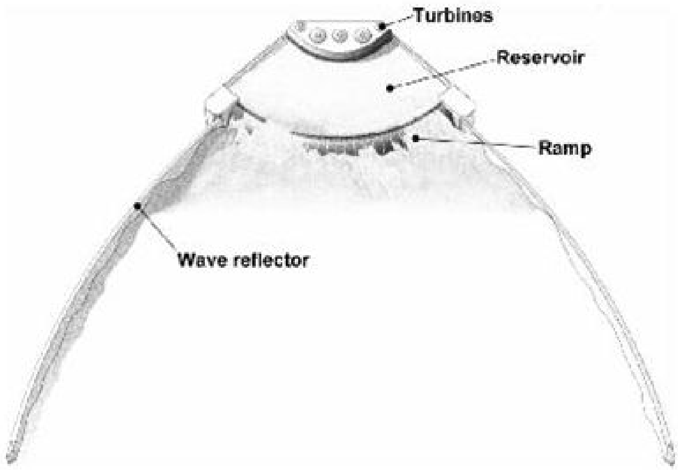

Figure 1.10 Overtopping Terminator the Wave Dragon [34]

Attenuator – sometimes called linear absorbers are long multi-segment floating structures oriented parallel to the direction of the waves. The differing heights of waves along the length of the device causes flexing where the segments connect, and this flexing is connected to hydraulic pumps or other converters [35] for instance the Pelamis [36], shown in Fig. 1.11, which is designed by Pelamis Wave Power Ltd. Another such device is the Irish McCabe Wave Pump [37] shown in Fig. 1.12, designed by Hydam Technology Ltd. The centre pontoon is attached to a submerged damper plate to hold it relatively still. The hydraulic pumps are attached between the centre and the end pontoons. Under the wave action the aft and forward pontoons move up and down. The pitching motion of the aft and forward floating pontoons pumps hydraulic fluid back and forth-motion that is used to drive a generator.

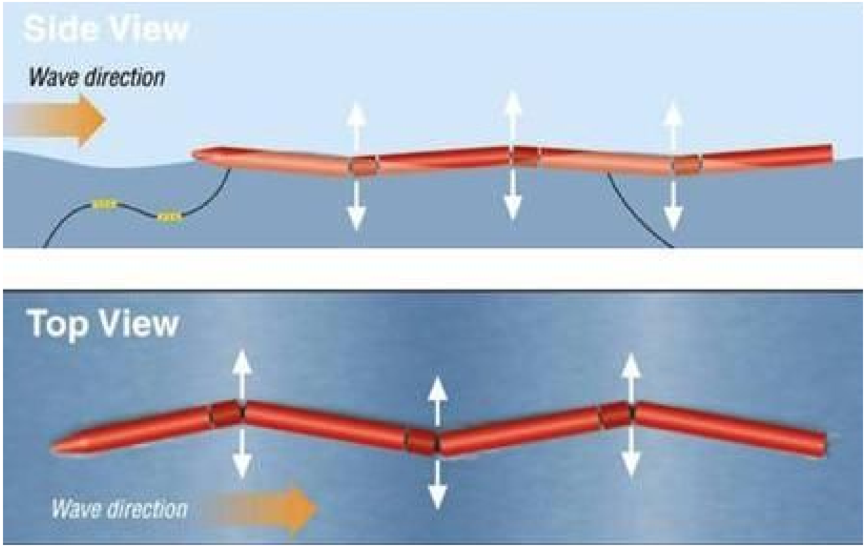

Figure 1.11 Pelamis Wave Energy Converter [38]

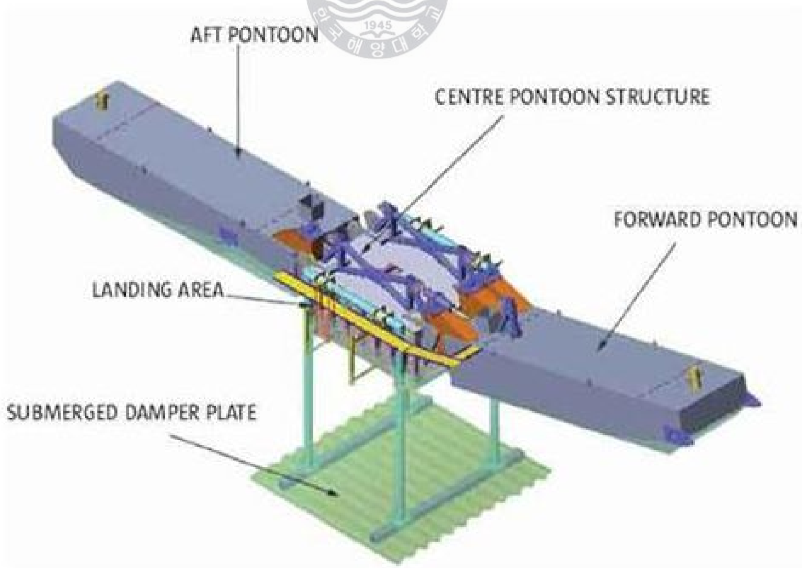

Figure 1.12 The McCabe Wave Pump [37]

Some of the wave energy converters (WEC) mentioned as well as some more devices is mentioned in Table 1.1.

Table 1.1 List of Wave Energy Devices [39]

Company Name	Device Name	Type of Technology
AWS Ocean Energy Ltd	Archimedes Wave Swing	Point Absorber
C-Wave	C-wave	Attenuator
Carnegie Corporation	CETO	Point Absorber
Checkmate Seaenergy	Anaconda	Attenuator
Energetech	Energetech	OWC
Finavera Renewables INC	AquaBuoy	Point Absorber
Green Ocean Energy Ltd	Ocean Treader WEC	Attenuator
JAMSTEC	Mighty Whale	OWC
Manchester Bobber	Manchester Bobber	Point Absorber
Oceanlinx	Denniss-Auld Turbine	OWC
Ocean Harvesting Technologies	Ocean Harvester	Attenuator
Ocean Power Technology INC	PowerBuoy	Point Absorber
Pelamis Wave Power Ltd	Pelamis	Attenuator
Wavebob Ltd	Wavebob	Point Absorber
Wave Dragon	WaveDragon	Overtopping
Wave Energy	Seawave Slot-Cone Generator	Overtopping
WAVEGEN	LIMPET	OWC
WavePlane Productions A/S	WavePlane	Overtopping

1.3 Motivation for Present Study

As discussed in section 1.2, there are varieties of wave energy devices in existence which can be employed to extract power form ocean surface waves. There is vast amount of knowledge gained and it can be further used to develop new devices or even improve on the existing devices. The current study pays attention to Oscillating Water Column (OWC). All the existing OWC's use air turbines for example Wells turbine to convert the pneumatic energy (compressed air) to electrical energy. The drawbacks to this type of turbine is the aerodynamic losses that occur at extreme sea conditions which eventually leads to big variation in the rotational speeds as well as noise in the turbine passages. To address this problem, Fukutomi et al [40] and Choi et al [41-42] have proposed a Direct Drive Turbine (DDT) which uses water as working fluid. With this being the motivation, the present study aims at using a DDT of the cross flow type (Banki Turbine) to generate power from ocean surface waves.

The DDT has many advantages; apart from cost effectiveness and ease of construction, it is also self cleaning, there is no problem of cavitation and its efficiency is much less dependent on the flow rate compared to other types of turbine [43]. The conceptual design of the caisson and the turbine system is shown in Fig. 1.13.

It is vital to point out that only flow characteristics are studied in the current work without the turbine in a Numerical Wave Tank (NWT). The waves in the numerical wave tank were generated by a piston type wave maker which was located at the wave tank inlet. The inlet which was modeled as a plate wall which moved sinusoidally with the general function, $x = a\sin\ wt$..

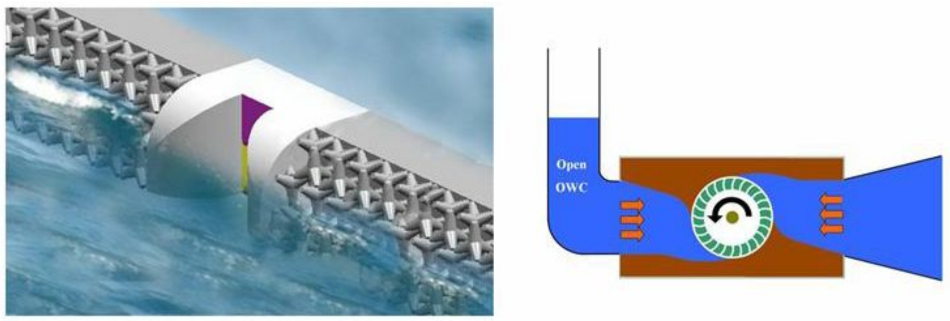

(a) Caisson (b) Caisson and Turbine

Figure 1.13 Conceptual Design of the Caisson (a) and the Turbine System (b)

There are three steps of wave energy conversion; primary energy conversion also known as first stage energy conversion, secondary energy conversion and tertiary energy conversion as shown in Fig. 1.14. However, only primary energy conversion is part of the present study. Design modifications were made to the base model for instance varying the front guide nozzle divergence angle, front guide nozzle configuration, augmentation channel geometry and rear chamber design to observe how these factors affect the available water power and hence the first stage energy conversion.

In addition to this, flow phenomenon such as flow separation and vorticity are also part of this study. The entire model that is solved by a commercial CFD code ANSYS-CFX includes the turbine section (front guide nozzle, augmentation channel and the rear chamber) and the NWT.

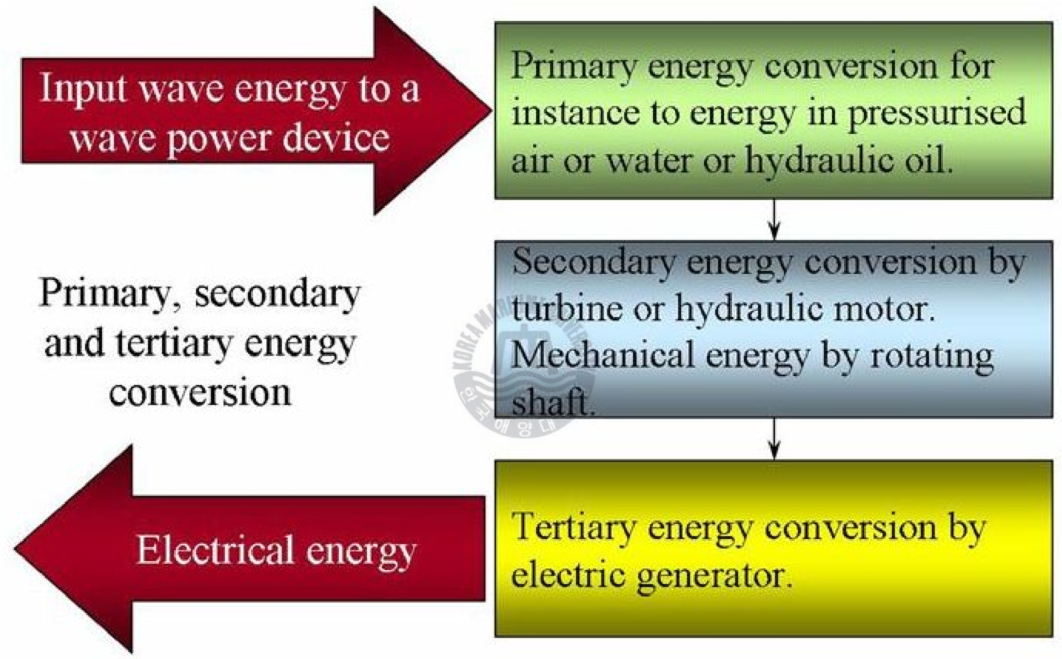

Figure 1.14 Steps of Wave Energy Conversion

CHAPTER 2 METHODOLOGY

2.1 CFD Code ANSYS-CFX and Turbulence Model

The use of numerical methods for example Computational Fluid Dynamics (CFD) in design process has increased significantly highlighting the rapid development in computer technology. For this project the commercial code of the ANSYS CFX Version 11 is used for simulation purposes. The sets of equation solved by ANSYS CFX are the unsteady Navier-Stokes equations in their conservation forms [44]. The instantaneous equations of mass (continuity equation) and momentum conservation are given in equations (2-1) and (2-2) respectively.

$$\frac{\partial \rho}{\partial t} + \nabla \bullet (\rho U) = 0 \tag{2-1}$$

$$\frac{\partial (\rho U)}{\partial t} + \nabla \bullet (\rho U \otimes U) = -\nabla p + \nabla \bullet \tau + S_M \tag{2-2}$$

where τ is the stress tensor.

However, for turbulent flows, the instantaneous equations are averaged leading to additional terms. In principle, the Navier-Stokes equations describe both laminar and turbulent flows without the need for additional information. However, turbulent flows at realistic Reynolds numbers span a large range of turbulent length and time scales. To predict the effect of turbulence, many turbulence models have been developed. In general, turbulence models seek to modify the original unsteady Navier-Stokes equations by the introduction of averaged and fluctuating quantities to produce the Reynolds Averaged Navier-Stokes (RANS) equations.

However, the averaging procedure introduces additional unknown terms containing products of the fluctuating quantities. These terms are called 'turbulent' or 'Reynolds' stresses. The Reynolds (turbulent) stress need to be modeled by additional equations of known quantities in order to achieve closure. To achieve closure means to have adequate amount of equations for all the unknowns including the Reynolds-Stress tensor. The equations used to close the system define the type of the turbulence model. The RANS equation is obtained by substituting the averaged quantities into the original transport equation, we obtain equations (2-3) and (2-4).

$$\frac{\partial \rho}{\partial t} + \nabla \bullet (\rho U) = 0 \tag{2-3}$$

$$\frac{\partial \rho U}{\partial t} + \nabla \bullet \{\rho U \otimes U\} = \nabla \bullet \left\{ \tau - \rho \overline{u \otimes u} \right\} + S_M \tag{2-4}$$

You can notice that the continuity equation remains unchanged but the momentum transport equation contains extra terms. These are the Reynolds Stress, $\rho \overline{u \otimes u}$ and the Reynolds flux, $\rho \overline{u \Phi}$

As mentioned earlier, turbulence models close the Reynolds-averaged equations by providing models for the computation of the Reynolds Stress and Reynolds fluxes. For the project this was achieved by using the k-ε model. The standard k-ε model [45] introduces two new variables into the equation system. One is for the computation of the turbulent kinetic energy, k, m^2/s^2; and the other is for the calculation of the turbulence eddy dissipation,ε, m^2/s^3. The following equation (2-5) is then obtained:

$$\frac{\partial \rho}{\partial t} + \nabla \bullet (\rho U) = 0 \tag{2-5}$$

And the momentum equation as shown in equation (2-6):

$$\frac{\partial \rho U}{\partial t} + \nabla \bullet (\rho U \otimes U) - \nabla \bullet (\mu_{eff} \nabla U) = -\nabla p' + \nabla \bullet (\mu_{eff} \nabla U)^T + B \tag{2-6}$$

where B is the sum of the body forces, μ_{eff} is the effective viscosity accounting for turbulence and p' is the modified pressure. The k-ε model is based on eddy viscosity concept, and the effective viscosity is then given by equation (2-7)

$$\mu_{eff} = \mu + \mu_t \tag{2-7}$$

The k-ε model assumes that the turbulence viscosity, μ_t ,is related to the turbulence kinetic energy and dissipation via the equation (2-8):

$$\mu_t = C_\mu \frac{k^2}{\varepsilon} \tag{2-8}$$

where C_μ is a constant.

The values of k and ε come directly from the differential transport equations for the turbulence kinetic energy, equation (2-9) and the turbulence dissipation rate, equation (2-10):

$$\frac{\partial(\rho k)}{\partial t} + \nabla \bullet (\rho U k) = \nabla \bullet \left[\left(\mu + \frac{\mu_t}{\sigma_k} \right) \nabla k \right] + P_k - \rho\varepsilon \tag{2-9}$$

$$\frac{\partial(\rho \varepsilon)}{\partial t} + \nabla \bullet (\rho U \varepsilon) = \nabla \bullet \left[\left(\mu + \frac{\mu_t}{\sigma_\varepsilon} \right) \nabla \varepsilon \right] + \frac{\varepsilon}{k}(C_{\varepsilon 1} P_k - C_{\varepsilon 2} \rho \varepsilon) \tag{2-10}$$

where $C_{\varepsilon 1}$, $C_{\varepsilon 2}$, σ_k and σ_ε are constants. P_k is the turbulence production due to viscous and buoyancy forces, which is modeled using equation (2-11):

$$P_k = \mu_t \nabla U \bullet (\nabla U + \nabla U^T) - \frac{2}{3} \nabla \bullet U (3\mu_t \nabla U + \rho_k) + P_{kb} \tag{2-11}$$

2.2 Numerical Setup

In the project, CFD work is conducted using ANSYS CFX. The first step of the project was to observe wave properties. This was achieved by using a Numerical Wave Tank (NWT). Waves in the NWT were generated using a piston type wave maker. Further details will be provided on this in the proceeding sections. Water wave motions are complex and irregular on the ocean surface. So in the NWT it was much easier to study 2-dimensional waves with parallel sidewalls where the boundary layer effect is very small, almost negligible. After the wave characteristics study in the NWT, the turbine section was incorporated into the calculation domain and the simulation was performed.

For the CFD simulation in ANSYS CFX, the process was broken down into few simple steps. These were:

- Creating the geometry, that is modeling.
- Meshing, that is grid generation.
- Defining the physics of the model, that is problem setup in CFX-Pre.
- Solving, CFX-Solver.
- Post processing, CFX-Post.

Each of the steps/process will be discussed in detail in the following sections.

2.3 Modeling

Three dimensional modeling of all the components were carried out using commercial software, UniGraphics NX 4. Please note that all the dimensions shown in the respective figures in this section are in millimeter (mm) unless specified. The entire model basically consisted of two major parts; the numerical wave tank and the turbine section. The length, width and height of the NWT was 15m, 1m and 1.5m respectively as shown in Fig. 2.1. The red section in Fig. 2.1 represents the moving mesh section. More on this will be explained in problem setup in CFX-Pre section. The turbine section, Fig. 2.2, consisted of:

- Front guide nozzle
- Front nozzle
- Rear nozzle
- Internal fluid region
- Rear chamber

The front nozzle and the rear nozzle were geometrically same. The front nozzle, rear nozzle and the internal fluid region forms the augmentation channel. The internal fluid region represents the turbine housing. The full model setup is shown in Fig. 2.3.

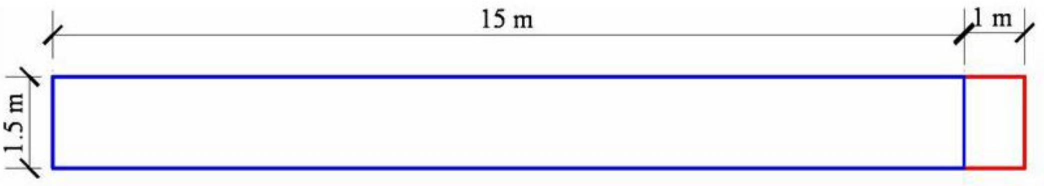

Figure 2.1 Dimensions for the Numerical Wave Tank

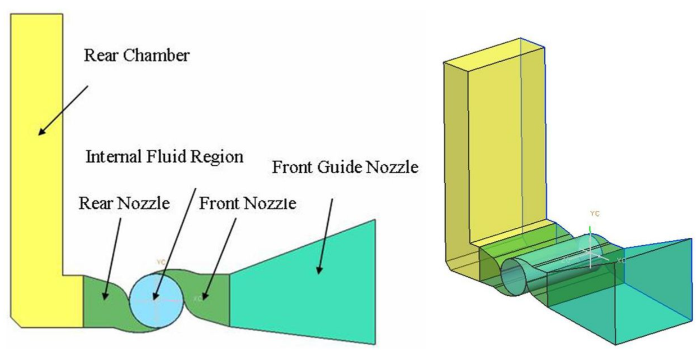

Figure 2.2 Turbine Section of Base Model

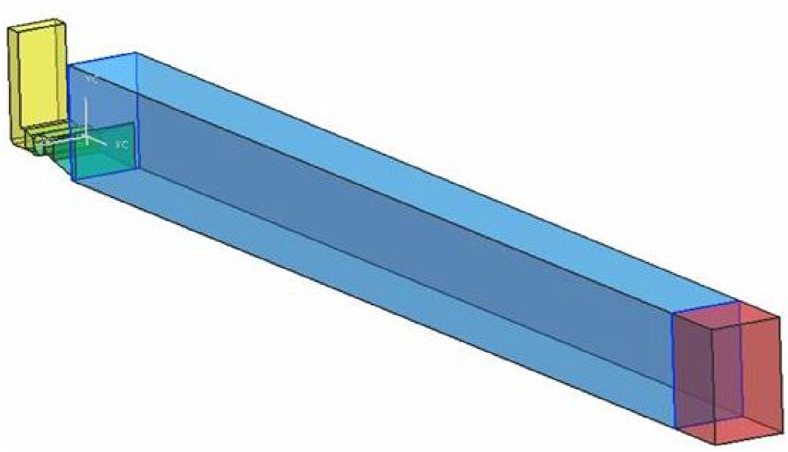
Figure 2.3 Full Model Setup

Modifications were made to the base model, specifically to the turbine section. The changes were made to the front guide nozzle, the augmentation channel (front nozzle and rear nozzle) and to the rear chamber. Each of the modifications is discussed in the following sub-section.

2.3.1 Front Guide Nozzle

For the front guide nozzle; effect of front guide nozzle divergence angle and front guide nozzle configuration on flow characteristics and water power were studied. The two different front guide nozzle divergence angles were $\alpha=0°$ (Red) and $\alpha=14°$ (Blue) as shown in Fig. 2.4. The one in blue is the base front guide nozzle (Guide 1). The front guide nozzle inlet width, W_G, for $\alpha=0°$ and $\alpha=14°$ was 700mm and 872mm respectively. Four additional front guide nozzle configurations with divergence angle of 14° were made. For these guide nozzles the inlet to outlet area ratio was kept constant at 3 as shown in Fig. 2.5.

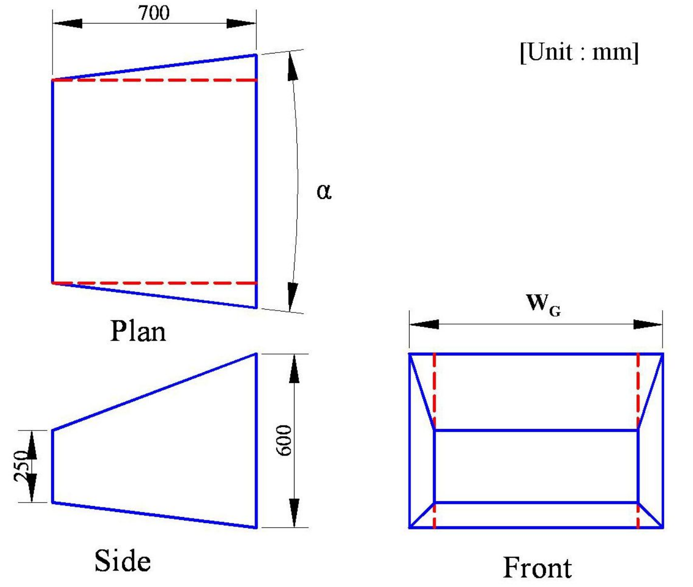

Figure 2.4 Front Guide Nozzle Dimension

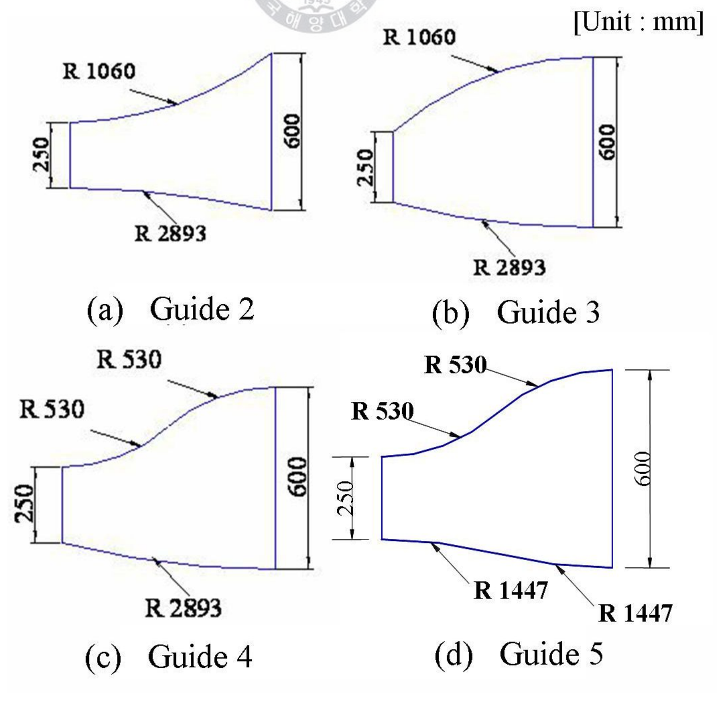

Figure 2.5 Additional Front Guide Nozzle Configurations

2.3.2 Augmentation Channel

A total of four additional different augmentation channel geometries were studied. As mentioned earlier, the augmentation channel consisted of front nozzle, rear nozzle and internal fluid region. Design changes were made to the front nozzle and rear nozzle only. The dimension for the base augmentation channel (Spiral Wall 1) is given in Fig. 2.6. The entrance arc is denoted as E_A, which was 105° in this case. The width of the channel was 700mm. Figure 2.7 shows the other four augmentation channel geometries that were used in the present project. The length, width and the inlet to outlet area ratio were kept the same for all the cases. Straight Wall augmentation channel was made as a control simulation to observe the effect of having the rear wall spiraled.

Other important variables studied were the entrance arc, E_A, and rear wall spiral design which is very important in determining the performance of the front nozzle and rear nozzle. Again attention is paid on the effect of augmentation channel geometry on flow characteristics and primary energy conversion (first stage energy conversion).

For design of rear wall of Spiral Wall 4 model equation (2-12) was used:

$$R_i = e^{\tan a_o [rad]} \times R_o \tag{2-12}$$

where R_i is the radius on the angle from the origin. The increment angle was 10°. e is the natural logarithm = 2.7183. a_o is the absolute entrance angle which was 16°. It is based on the runner inlet angle and for this case it is designed for runner inlet angle of 30° calculated using Banki theory. *rad* is the incremental angle in radians. R_0 is the base radius (runner radius) = 130mm.

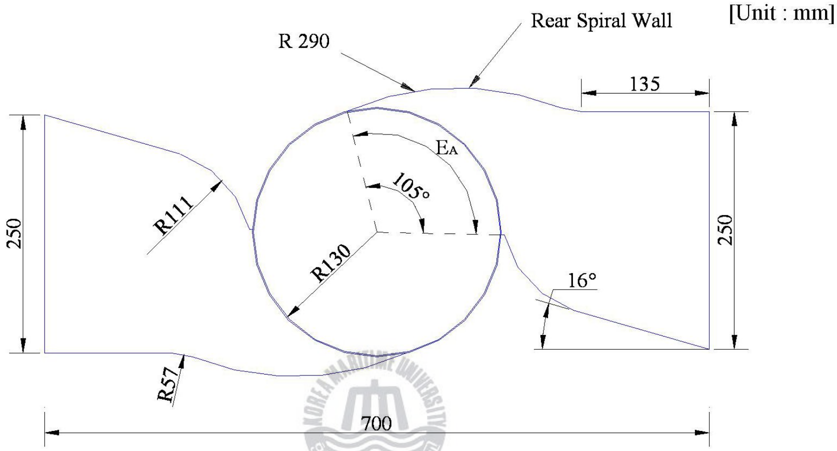

Figure 2.6 Base Model Augmentation Channel Dimension (Spiral Wall 1)

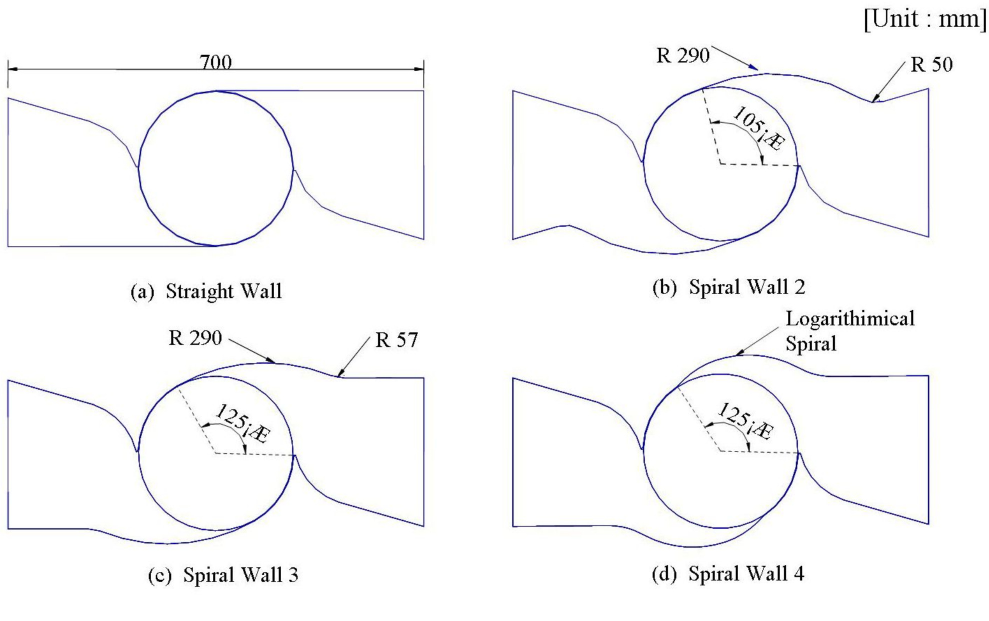

Figure 2.7 Additional Augmentation Channel Geometries

2.3.3 Rear Chamber

Rear chamber is the last attachment and the water oscillates here. The height of the rear chamber was 1.5m. The dimension for the base rear chamber is given in Fig. 2.8.

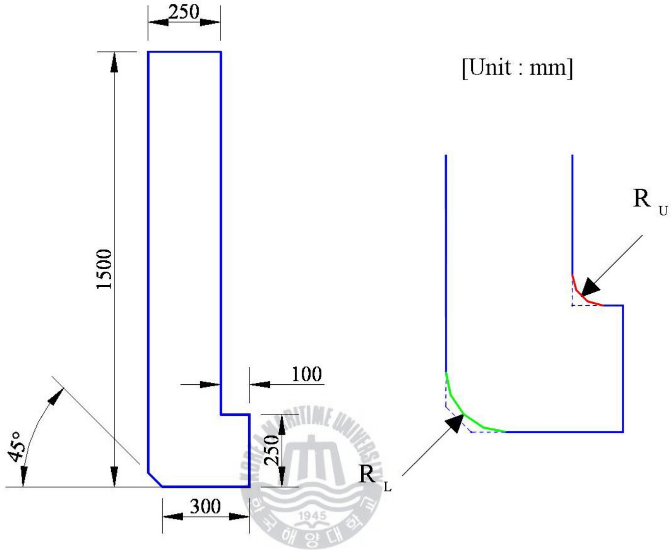

Figure 2.8 Rear Chamber Dimension (Base Model)

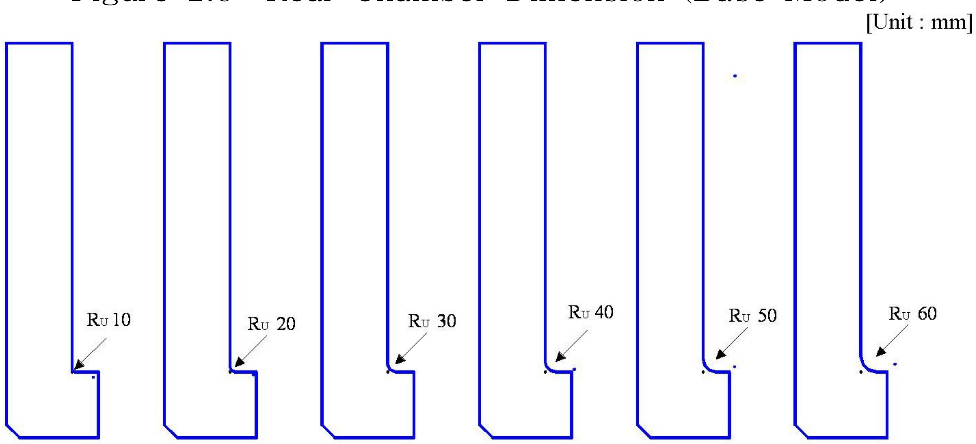

Figure 2.9 Upper Corner Modifications

Several modifications were made to the rear chamber. The upper sharp corner was filleted as shown on the figure on the right in Fig. 2.8 in red. R_U is the upper corner fillet radius. The modification to the upper corner is given in Fig. 2.9. The rear bottom wall of the chamber was also modified as shown in green in Fig. 2.8. R_L is the lower corner fillet radius and the rear bottom wall modification is given in Fig. 2.10.

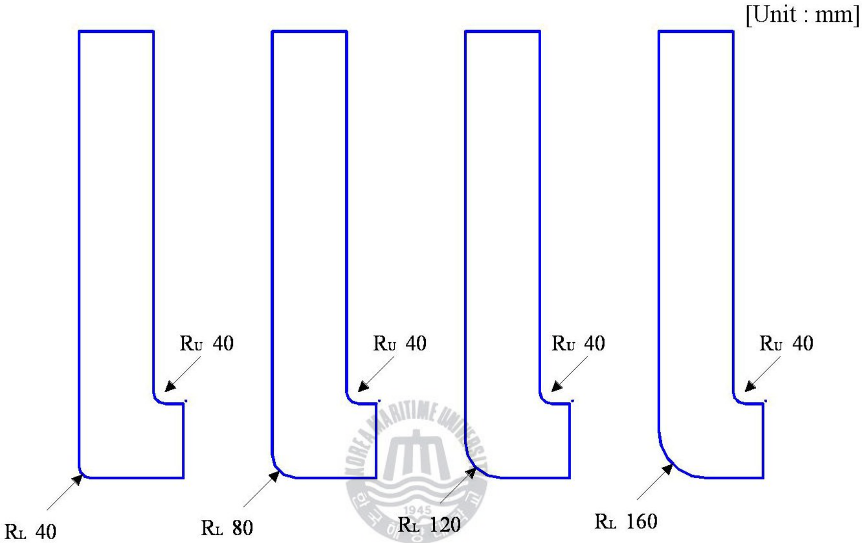

Figure 2.10 Rear Bottom Wall Modifications

2.4 Grid Generation

Computational grid is generated using ANSYS ICEM – CFD. The computational domain is discretized with hexahedral grid. Hexahedral volume meshes are used to ensure the obtained result is of highest quality that is, high accuracy. Due to the complexity of the model, the entire model was broken down into four major components. These were NWT, front guide nozzle, augmentation channel and the rear chamber. Furthermore, the augmentation channel was broken down into front nozzle, rear nozzle, top strip, bottom strip and internal fluid region. The grid generation for front guide nozzle and the rear chamber is shown in Fig. 2.11. Figure 2.12 shows mesh generation for the numerical wave tank.

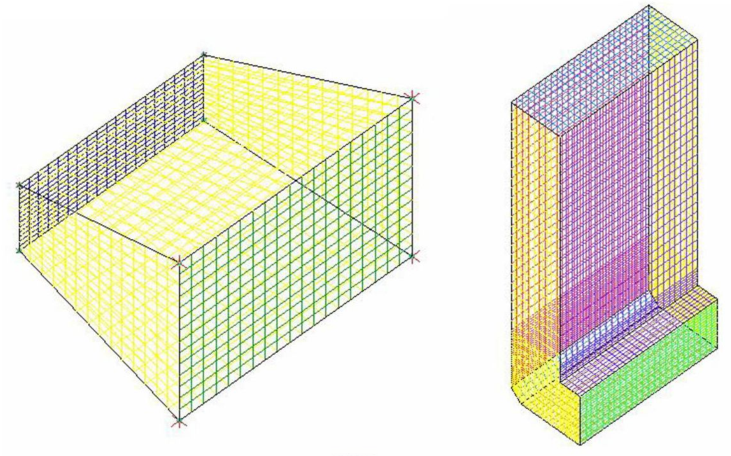

(a) Front Guide Nozzle (b) Rear Chamber

Figure 2.11 Mesh Generation for Front Guide Nozzle (a) and Rear Chamber (b)

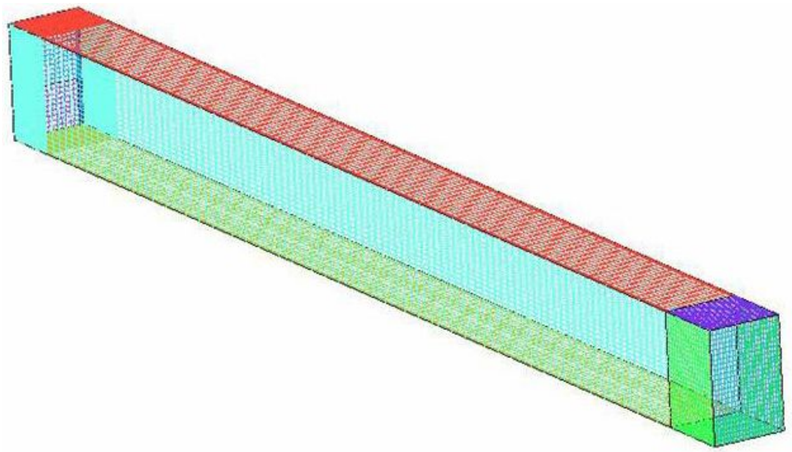

Figure 2.12 Mesh Generation for NWT

Grid generation for the various parts for the augmentation channel is given in Fig. 2.13. The front nozzle and the rear nozzle are geometrically same as well as the top strip and the bottom strip. The combined mesh for the augmentation channel (base model) and the turbine section (base model) is shown in Fig. 2.14. The number of nodes for each component is given in Table 2.1. The number of nodes for all the models studied in the present work was kept approximately the same.

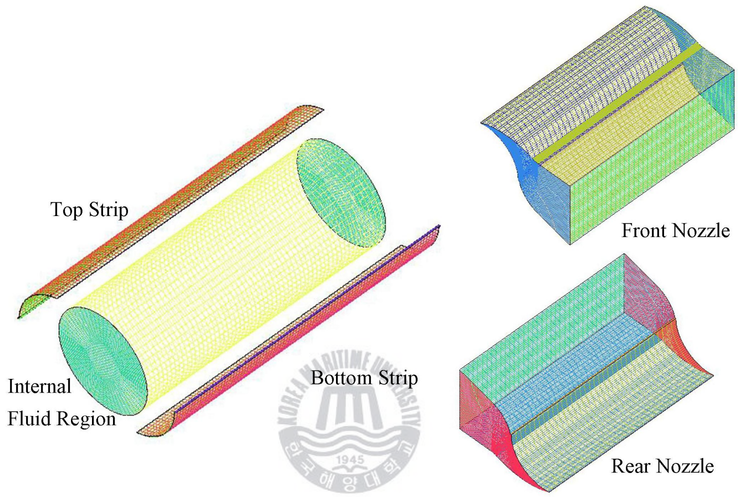

Figure 2.13 Mesh Generation for the Parts in the Augmentation Channel (Base Model)

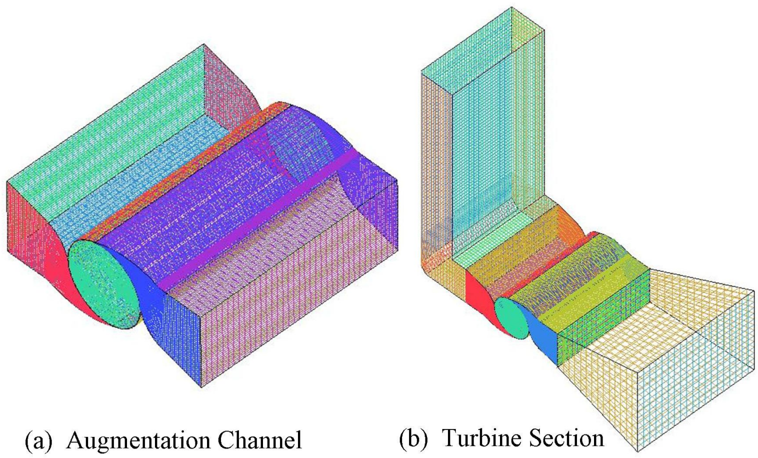

Figure 2.14 Combined Mesh Generation for Augmentation Channel (a) and Turbine Section (b) for the Base Model

Table 2.1 Nodes for Each Component

Component	Nodes
Numerical Wave Tank	78936
Front Guide Nozzle	15750
Augmentation Channel	
Front and Rear Nozzle	243460
Top and Bottom Strip	32760
Internal Fluid Region	94140
Rear Chamber	28980
TOTAL	494026

2.5 Problem Setup in CFX-Pre

Upon completion of grid generation, the individual components were imported to ANSYS CFX Pre. The physical models that are to be included in the simulation are selected. Fluid properties and boundary conditions are specified. The waves in the numerical wave tank were generated by the piston type wave maker which was located at one end of the NWT. This was accomplished by incorporating a moving mesh section in the NWT. The wave maker plate was assigned a sinusoidal motion with the general formula given as in equation (2-13).

$$x_{dis} = A \sin \omega t \tag{2-13}$$

where x_{dis} is displacement of the wavemaker plate in x-direction, A is the amplitude, ω is the frequency and t is the simulation time-step. Figure 2.15 shows the schematic of the numerical wave tank. This is a multi-phase simulation where there is two phase present namely water and air. To capture the air-water interface, Volume of Fluid (VOF) method was used [46]. Let V_W be the volume fraction of water and V_A be the volume fraction of air. For any given computational cell, the volume fraction of water and air sum should be equal to 1. If we take V_W, then there is 3 possible conditions; ($V_W=1$), the cell is full of water, ($V_W=0$), cell is empty of water and ($0<V_W<1$), the cell contains the interface that is, the free surface interface having both water and air.

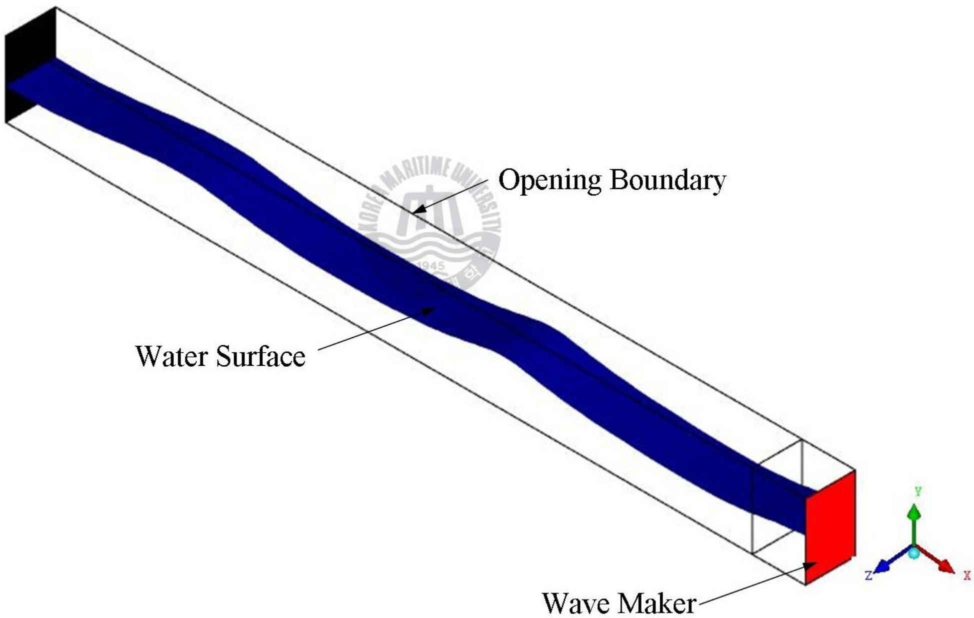

Figure 2.15 Schematic of the Numerical Wave Tank

An unsteady simulation (transient) was performed based on Reynolds averaged Navier-Stokes (RANS) equation with k-ε turbulence model. The time discertization of the equations was achieved with the implicit second order Backward Euler scheme for time-step of 0.05s [47]. The computational grid was divided into five domains; moving mesh section, NWT, front guide nozzle, augmentation channel and the rear chamber as shown in Fig. 2.16.

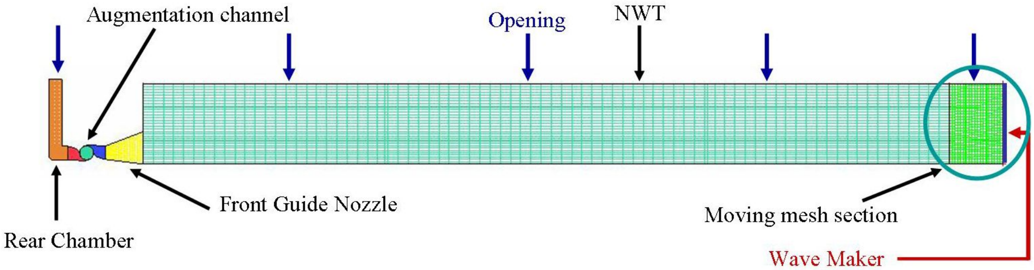

Figure 2.16 Computational Domain

The right hand boundary is the wave maker plate which moved sinusoidally with a specified displacement. The side walls and the bottom wall of the moving mesh section were modeled as walls with unspecified mesh motion. The top wall of the moving mesh section, NWT and the rear chamber was open to the atmosphere hence; the boundary condition was set as opening with relative pressure set to 0 Pa. The rest of the outside walls of the computational domain were modeled as solid walls where no-slip boundary condition is applied. The no-slip condition ensures that the fluid moving over the solid surface does not have a velocity relative to the surface at the point of contact. Lastly, appropriate interface regions were created. For interface, the mesh connection method was automatic. Table 2.2 summarizes the CFX-Pre conditions.

Table 2.2 ANSYS CFX-Pre Conditions

Condition	
Simulation Type	Transient
Turbulence Model	k-ε
Phase	Water and Air at 25°C
Density	Water = 997 kg/m3 Air = 1.18 kg/m3
Time-step	0.05 s
Surface Tension Coefficient	0.075 N/m
Interface Type	Fluid to Fluid
Interface Length Scale	1 mm
Wave Maker	Piston Type
Opening	1 atm
Walls	No-slip Condition

2.6 CFX-Solver

The component that solves the CFD problem is called the Solver. It produces the required results in a non-interactive batch process. The CFX Version 11 is based on the Finite Volume Method (FVM). The first step in the FVM is to divide the domain into a number of control volumes (also known as cells or elements) where the variable of interest is located at the centroid of the control volume [48]. The next step is to integrate the differential form of the governing equations (very similar to the control volume approach) over each control volume. Interpolation profiles are then assumed in order to describe the variation of the concerned variable between cell centroids. The resulting equation is called the discretization equation. In this manner, the discretization equation expresses the conservation principle for the variable inside the control volume. Figure 2.17 shows a vertex centred FVM technique.

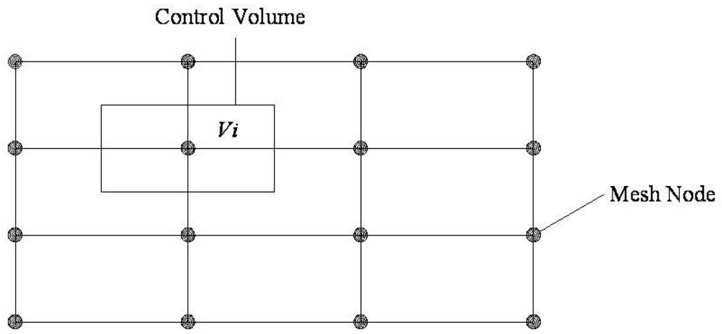

Figure 2.17 Vertex Centred FVM Technique

2.7 CFX-Post

The CFX-Post (post processor) users the result file which is made by CFX-Solver. The post-processor is the component used to analyze, visualize and present the results interactively. Post-processing includes anything from obtaining point values to complex animated sequences. Examples of some important features of post-processors are:

- Visualization of the geometry and control volumes.
- Vector plots showing the direction and magnitude of the flow.
- Visualization of the variation of scalar variables.
- Quantitative numerical calculations.
- Animation.
- Charts showing graphical plots of variables.
- Hardcopy output.

CHAPTER 3 RESULTS AND DISCUSSION

3.1 Overview

The results are presented in this section. Results are divided into sections and the effect of each modification for instance front guide nozzle shape, augmentation channel geometry and rear chamber design on flow characteristics and primary energy conversion is discussed. These sections are as listed below:

- Numerical wave tank simulation results
- Front guide divergence angle
- Simulation at different wave period
- Front guide nozzle shape
- Rear chamber design
- Augmentation channel geometry
- Best model (Final Model) simulation and comparison

It is important to mention again that only flow characteristics and primary energy conversion is part of this project. There is no runner included in the calculation domain. Flow characteristics in the front guide nozzle, the augmentation channel and rear chambers are studied for various models. It is important to deal with issues related to primary energy conversion. The power output from the system can be increased in two ways; either by making changes to the system to increase the primary energy and hence meaning more power available for the runner. The other is by optimizing the design of the runner itself to increase turbine efficiency; that is the secondary energy conversion.

To achieve higher primary energy conversion, the front guide nozzle, augmentation channel and the rear chamber design was optimized. From each individual optimization, the best model was obtained and the overall performance of this model was compared with the base model. In addition to this, simulation for varying wave period was also conducted. This was done in order to investigate the effect of wave parameters on the power available in waves. The power in waves is proportional to the square of significant wave height and the wave period.

3.2 Numerical Wave Tank

For wave generation a numerical wave tank was employed as described in section 2.5 of the methodology. Figure 3.1 shows the wave height profile in the NWT for a time period of approximately 25s at a point in the middle of the wave tank. Corresponding to this point the mean velocity was 0.2m/s. The location of this point is such that it lies in line with the centre of the internal fluid region.

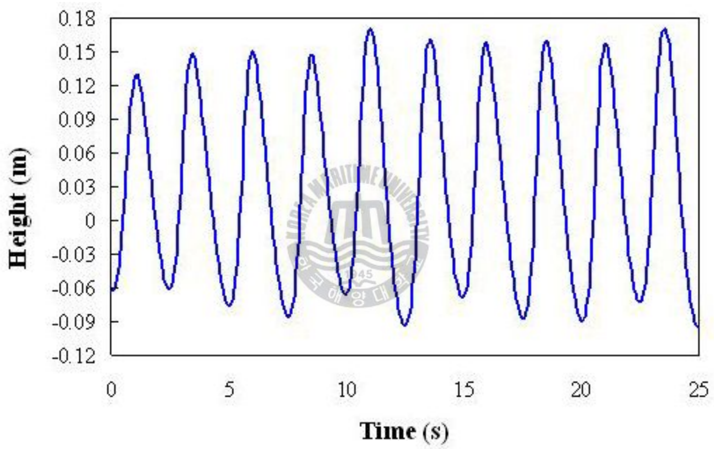

Figure 3.1 Water Wave Height in the NWT

Formation of waves in the NWT is shown with the help of volume fraction in Fig. 3.2. In Fig. 3.2, red shows water and blue represents air. The air/water free surface is shown in yellowish colour. When the free surface is disturbed, waves are formed. Theses waves are sometimes called gravity waves, because it is caused by the force of gravity tending to bring the surface to its equilibrium position. Due to momentum, it overshoots the mean position and hence oscillates and the disturbance is spread to neighboring portion of the surface.

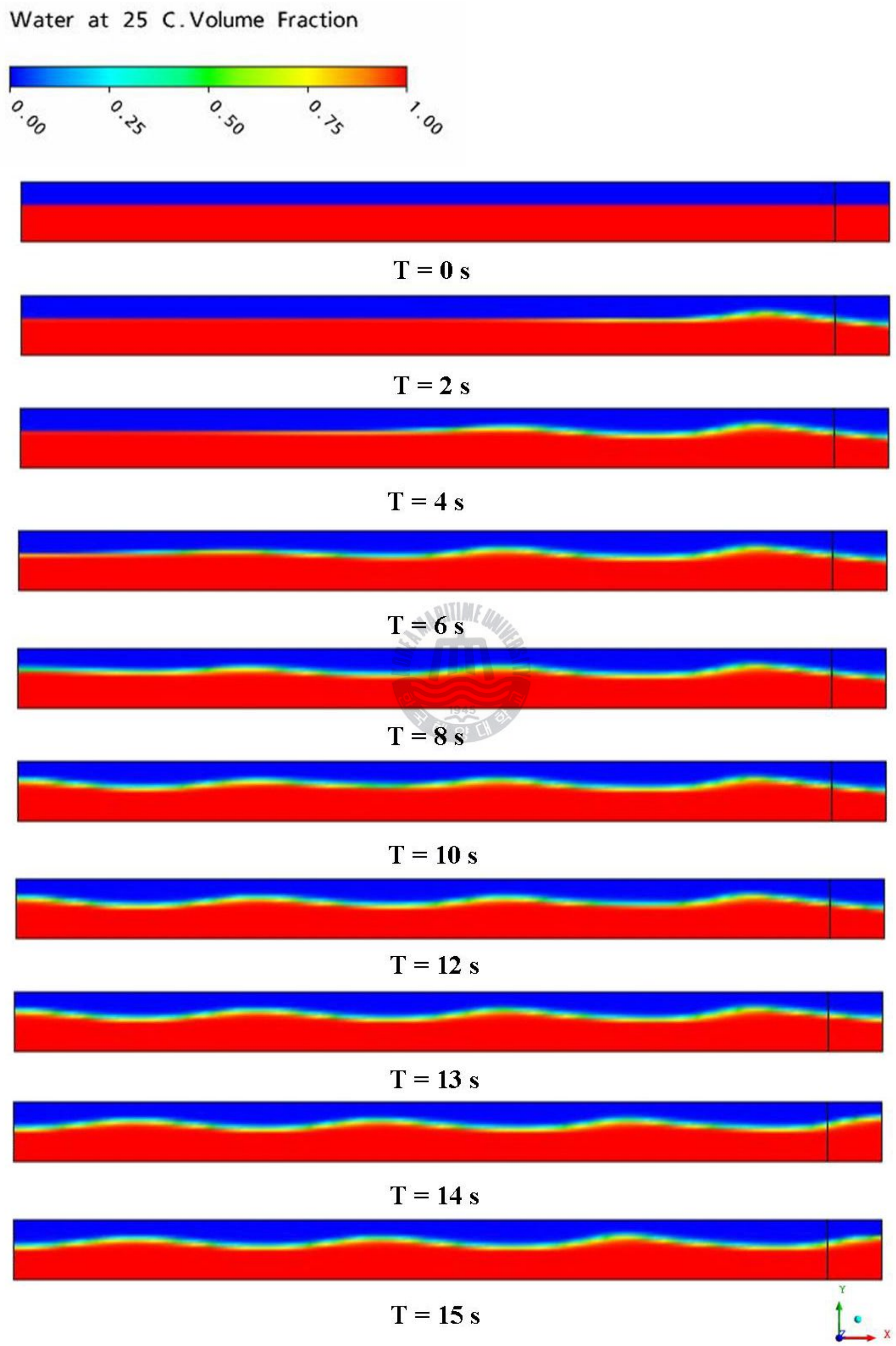

Figure 3.2 Volume Fraction Showing Formation of Waves in the NWT

The water velocity in the NWT is shown in Fig. 3.3. As expected, kinetic energy is concentrated at the surface and the velocity decreases with increasing depth. Another observation made was that the velocity slightly decreased as the waves traveled towards the back wall.

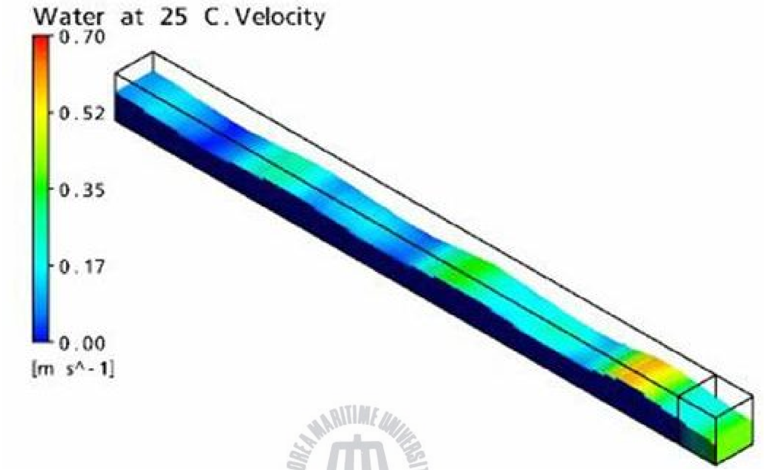

Figure 3.3 Water Velocity in the NWT

Table 3.1 Wave Parameters

Parameter	Value
Wave Height (H)	0.23 m
Wave Period (T)	2.5 s
Wavelength (λ)	6.3 m
Water Depth (d)	0.75 m
Mean Velocity (v_t)	0.2 m/s

Table 3.1 shows the wave parameters in the NWT. Using water depth and the wave length, it was determined using the criteria that the wave propagation was in intermediate water depths, $(0.05\lambda < d < 0.5\lambda)$ and the power in the incoming waves was calculated respectively using the intermediate water wave

equations as given in equations (3-1) to (3-4).

$$c_p = \sqrt{\frac{g\lambda}{2\pi}\tanh\left(\frac{2\pi d}{\lambda}\right)} \quad [m/s] \tag{3-1}$$

$$c_g = \frac{1}{2}c_p\left(1+\frac{4\pi d}{\lambda}\frac{1}{\sinh\left(\frac{4\pi d}{\lambda}\right)}\right) \quad [m/s] \tag{3-2}$$

$$E = \frac{1}{16}\rho g H^2 \quad [J/m^2] \tag{3-3}$$

$$P_{Wave} = Ec_g \quad [W/m] \tag{3-4}$$

where c_p is the phase velocity, c_g is the group velocity, g is acceleration due to gravity, ρ is the water density, E is the energy density per unit area and P_{Wave} is the wave energy flux or wave power. Making appropriate substitutions in the equations, the wave energy flux in the incoming waves was, P_{Wave}=68.6W/m. Pressure in the NWT is shown by means of pressure contour as shown in Fig. 3.4 and as expected the pressure increases with water depth.

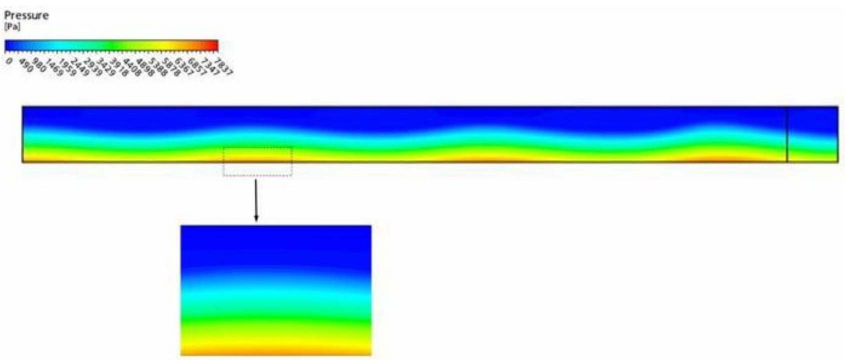

Figure 3.4 Pressure Contour in the NWT

3.3 Front Guide Nozzle Divergence Angle

Two different front guide nozzle divergence angle were studied, α=0° and α=14°. The purpose of this study was to see how the divergence angle affects the flow characteristics and the water power. Velocity vector in the mid-plane (XY plane at z = 0) for α=14° is shown in Fig. 3.5. As the waves approach the back wall, the flow is directed into the front guide nozzle. It is interesting to see that the flow pattern near region 1. The water is funneled into the guide nozzle and as the water flows through the nozzle, it gains kinetic energy. At section 2, high velocity is recorded and it changes position when water is flowing out of the front guide nozzle.

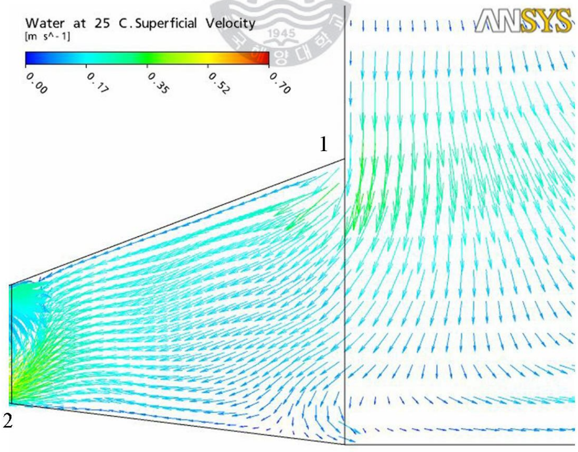

Figure 3.5 Velocity Vector in the Front Guide Nozzle and NWT in XY Plane at z = 0

The velocity recorded at the front guide nozzle inlet was 0.09 m/s which corresponds to a decrease of approximately 55% when compared to the 0.2m/s velocity recorded in the

NWT. This decrease in velocity is due to the flow resistance offered by the augmentation channel which forces the incompressible flow to divert from the augmentation channel.

Figure 3.6 shows the velocity vector in the XZ plane at y = 0 in both the front guide nozzles when water is entering. It is seen that for α=0° when water enters the front guide nozzle, due to sudden contraction there is obstruction and as a result the flow modifies and there is flow separation. For α=14° the flow is guided smoothly into the front guide nozzle which results in better performance.

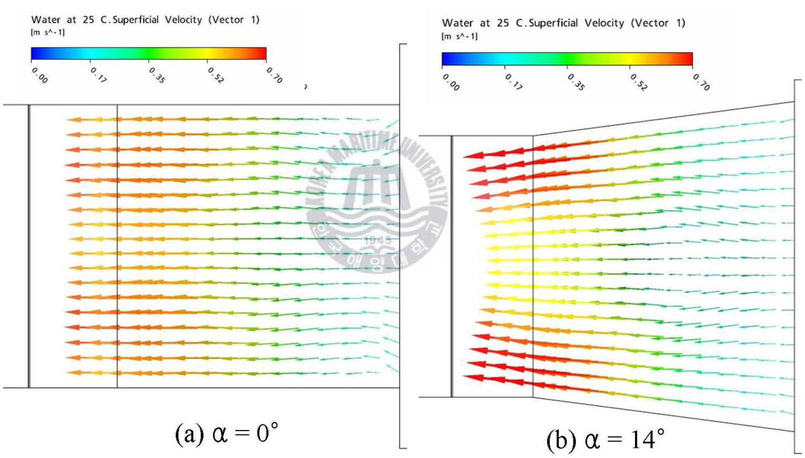

Figure 3.6 Velocity Vector in the Front Guide Nozzle in XZ Plane at y = 0 for (a) 0° and (b) 14° divergence angle

Since the front guide nozzle is symmetric about the x-axis, monitoring points were assigned to half the section as shown in Fig. 3.7. $z/W_{oi}=0$ is the centre and $z/W_{oi}=1$ is a point on the sidewall. W_{oi} is the cross sectional width at section *i* that is at section 1 to 3. The results show that having the front guide nozzle divergent is advantageous. The velocity recorded for α=14° is 10% higher than that in α=0°.

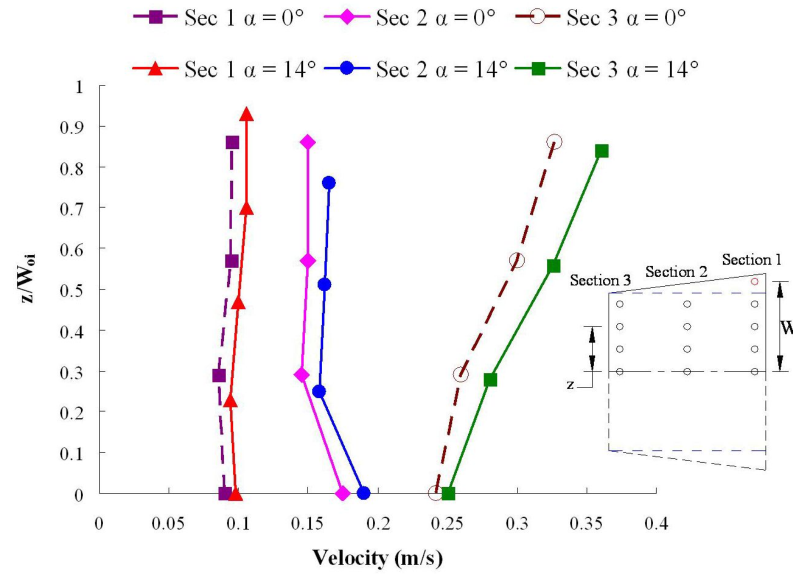

Figure 3.7 Velocity in the Front Guide Nozzle in XY Plane at $z = 0$

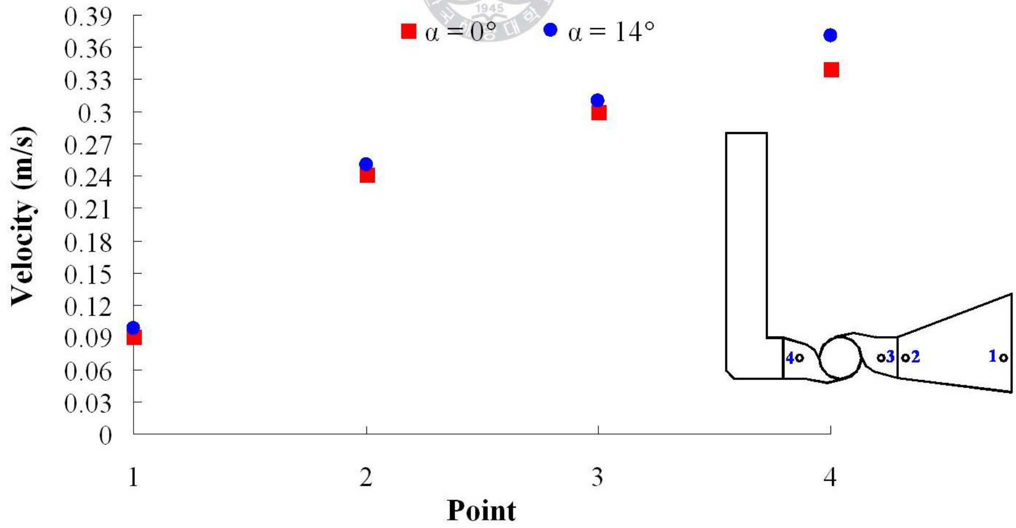

Figure 3.8 Average Velocity at Points 1 to 4

The average velocity recorded in the front guide nozzle (points 1-2) and the front nozzle (point 3) and rear nozzle (point 4) is given in Fig. 3.8. There is a decrease in the velocity at the inlet of the front guide nozzle but it gradually increases along the guide nozzle. The flow is the augmentation channel is also affected by the divergence angle of the front guide nozzle. For α=14° the average velocity recorded in the front nozzle and the rear nozzle is about 8% higher than that recorded in α=0°.

The water power is calculated using equation (3-5).

$$P_{WP} = \rho g Q \Delta H \qquad [\mathrm{W}] \qquad (3\text{-}5)$$

$$Q = \frac{V}{T} = \frac{A_{CS} \times (2\Delta Y)}{T} = \frac{2A_{CS}\Delta Y}{T} \qquad [\mathrm{m^3/s}] \qquad (3\text{-}6)$$

$$P_{Avail} = P_{Wave} \times W_G \qquad [\mathrm{W}] \qquad (3\text{-}7)$$

$$C_f = \frac{P_{WP}}{P_{Avail}} \qquad (3\text{-}8)$$

ΔH in equation (3-5) is the head difference across the front nozzle and the rear nozzle that is across point 3 and 4 as shown in Fig. 3.9. In equation (3-6), Q is the volume flow rate. A_{CS} is the rear chamber cross sectional area which was $0.175\mathrm{m}^2$. ΔY is the rear chamber water level difference. For the given period T, there are two oscillations in the rear chamber that is, the water level rises to a maximum and then falls to a minimum so displacing twice the volume and that is why multiplying ΔY by 2 in equation (3-6). The available power at the front guide nozzle inlet is given by equation (3-7). The front guide nozzle inlet width is denoted by $W_{G.}$ C_f is the first stage energy conversion factor or the primary energy conversion factor is given by equation (3-8). The water power, P_{WP} was non dimensionalized with the power available at the front guide nozzle inlet, P_{Avail}. For α=14° and α=0° , P_{Avail} was 60W and 48.2W respectively.

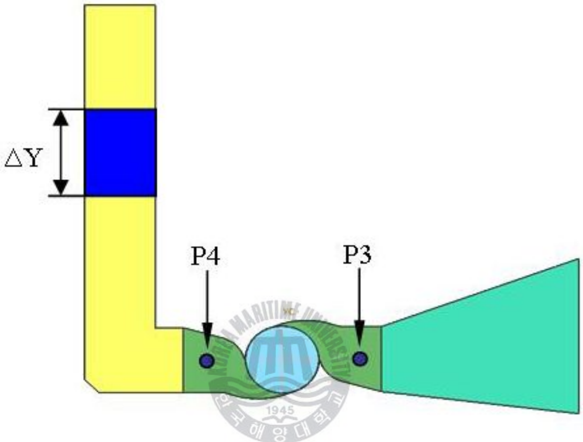

Figure 3.9 Power Calculation Formulation

Water power (P_{WP}) recorded for α=14° was 29.9 W and for α=0° it was 24.1 W which corresponds to an increase of 19%. However, the primary energy conversion remained fairly same, C_f for α=0° and α=14° was 0.50. We are just increasing the wave front power by making the front guide divergent which results in the increase in the water power for α=14°. It is important to note that increasing the divergence angle will not necessary increase the water power because beyond certain angle of divergence, flow separation will occur which will eventually lead to decrease in the water power. So in simple at the same wave condition, by having a larger front guide nozzle inlet width, the water power can be increased. Higher water power means that more power is available to the runner and this in turn will lead to higher turbine output. Further modification was made to the, α=14° front guide nozzle and the results of these changes are mentioned in section 3.5 of this chapter.

3.4 Simulation at Different Wave Periods

A total of five different wave periods were chosen. It was between 2s to 3s with increments of 0.25s. The objective was to see how different wave conditions affect the wave power and hence the water power of the system.

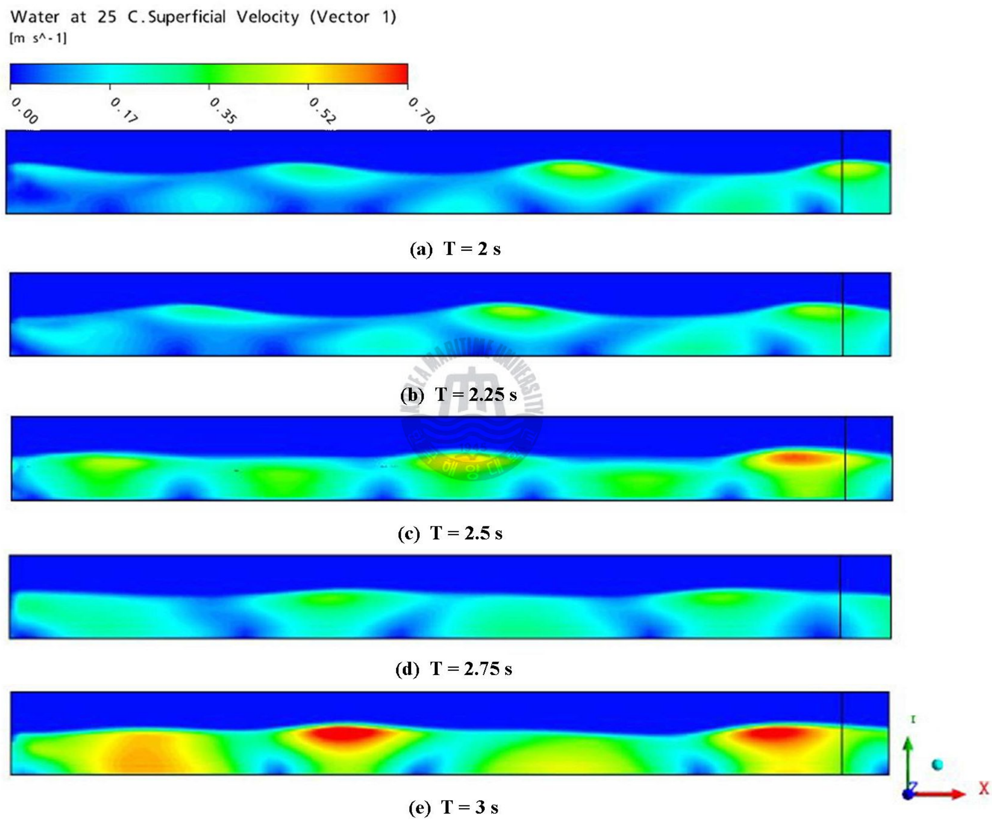

Figure 3.10 Velocity Contour in the NWT at Different Wave Periods

In Fig. 3.10 the superficial velocity contour in the numerical wave tank is shown for the time instant when the wave maker is pushing the water towards the back wall that is, it has moved to its maximum position in negative x - direction. High energy flow is observed as the wave period increases from 2s to 2.5s. However, for T=2.75s, the kinetic energy is lower than that recorded for wave period of 2.5s. As for T=3s, it recorded the highest velocity and in Fig. 3.11 the average velocity in the middle of the NWT is shown.

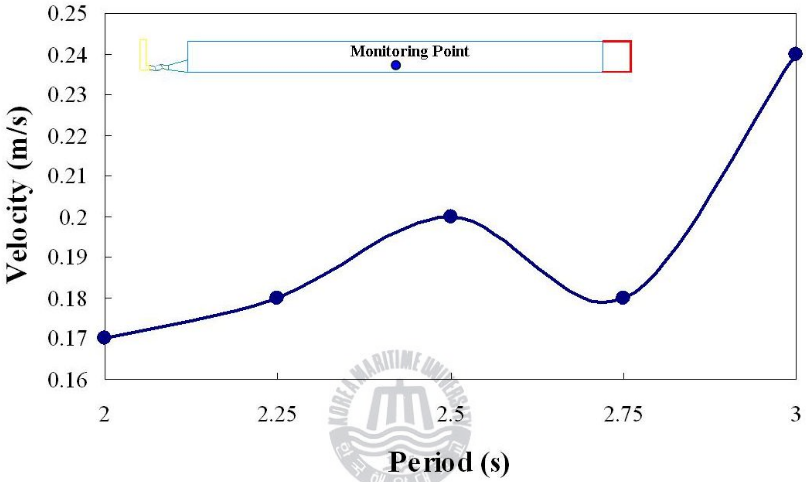

Figure 3.11 Average Velocity at the Middle of the NWT for Different Wave Periods

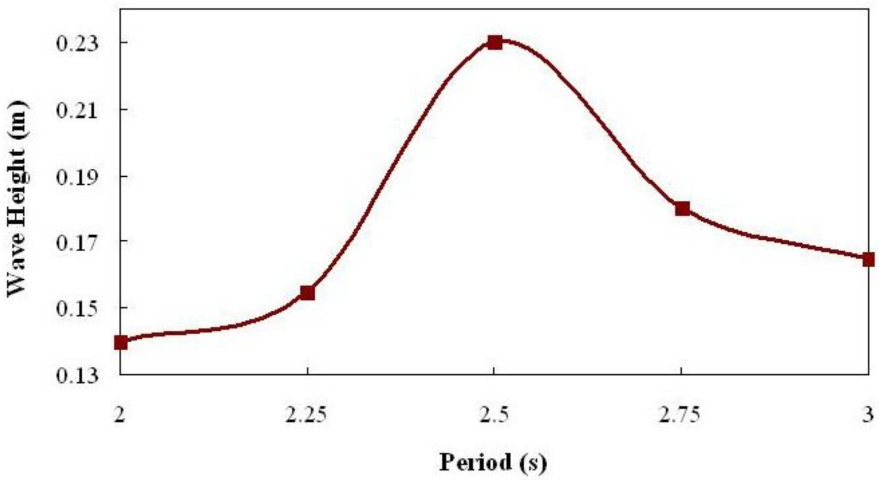

Figure 3.12 Wave Height in the NWT at Different Wave Periods

The wave height at different wave period is shown in Fig. 3.12. It is generally seen that as the wave period decreases the wave height increases however this was not the case in the present study. The peak occurs as wave period of 2.5s. There is an increase in the wave height as the period decreases from 3s to 2.5s. From 2.5s onwards to 2s the wave height decreases significantly. This decrease could be due to wave breaking which reduces the height.

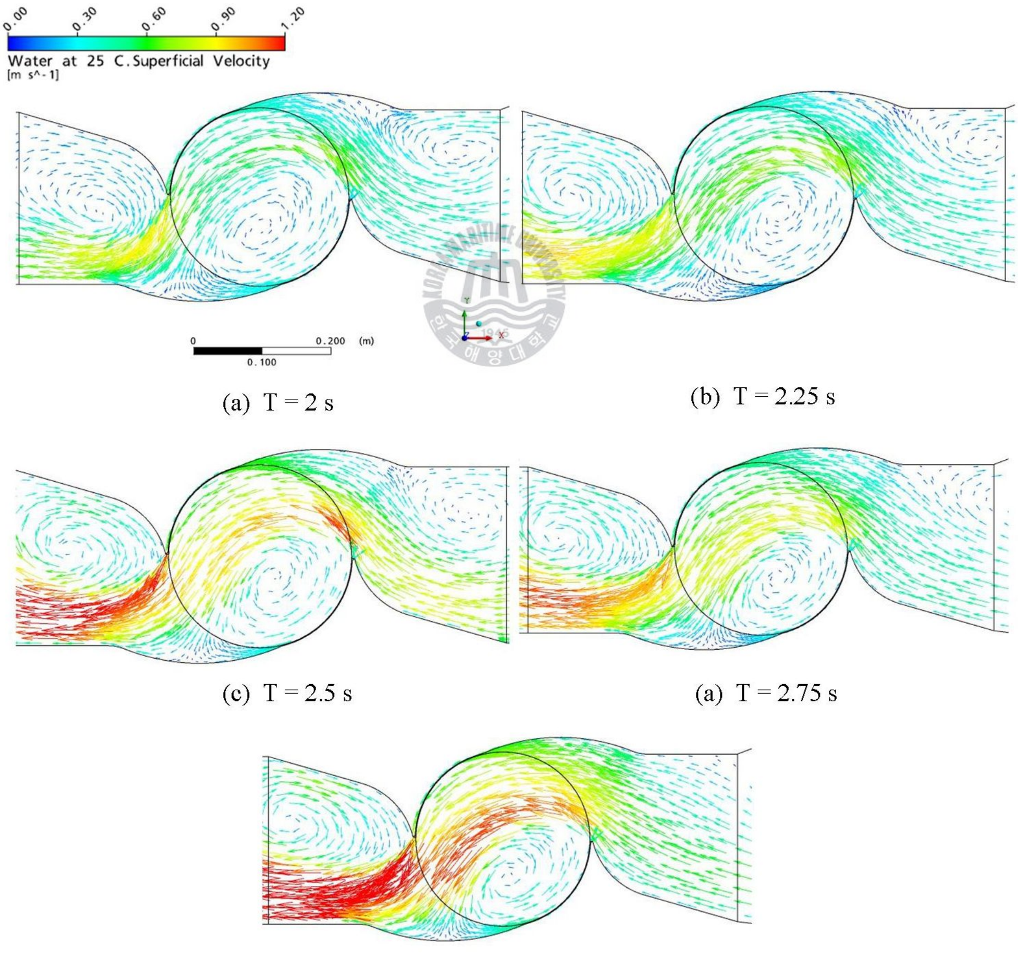

(a) T = 2 s

(b) T = 2.25 s

(c) T = 2.5 s

(a) T = 2.75 s

(e) T = 3 s

Figure 3.13 Velocity Vector in the Augmentation Channel at Different Wave Periods

Velocity vector in the augmentation channel is given in Fig. 3.13. It is shown at the instant when water is flowing into the augmentation channel. From Fig. 3.13 it is clear that the highest velocity in the augmentation channel was recorded for T=3s. The velocity increases from T=2s to T=2.5s, however at T=2.75s there is a decrease. This could be due to flow modification up stream in the front guide nozzle and hence affecting the performance of the augmentation channel.

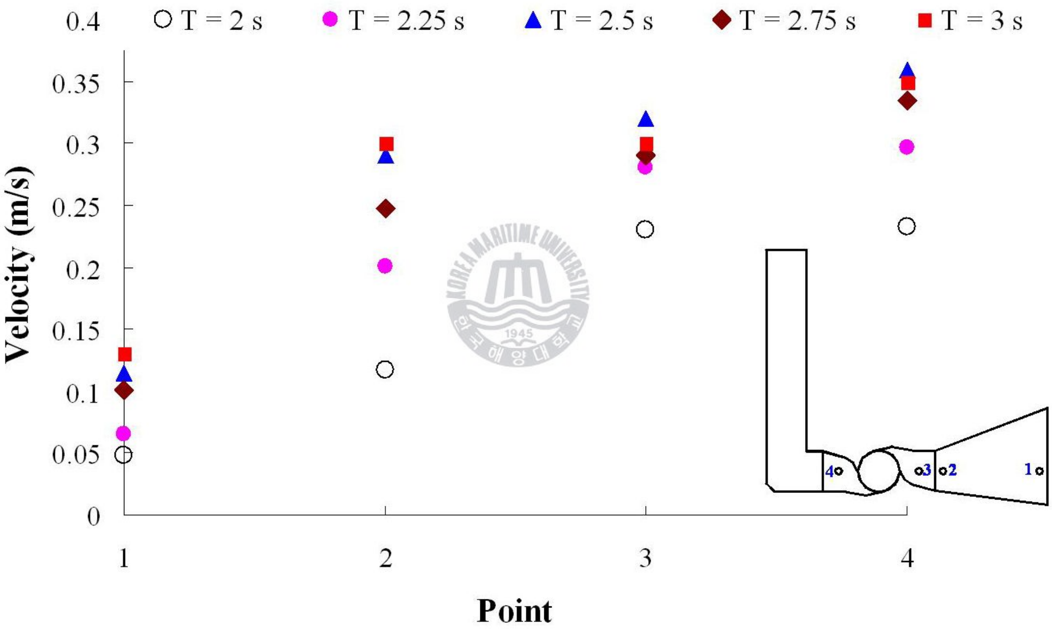

Figure 3.14 Average Velocity at Points 1 to 4 at Different Wave Periods

The average velocity at points 1 to 4 is shown in Fig. 3.14. The average velocity record in the front guide nozzle is highest for wave period of 3s but it is interesting to see that in the front nozzle and the rear nozzle, the highest velocity is recorded for T=2.5s. This is contradictory to what is observed in Fig. 3.13. The increase could be due to better flow characteristics in the augmentation channel at T=2.5s. The velocity recorded increases with wave period however, at T=2.75s there is slight decrease when compared to T=2.5s and fairly low velocity was recorded for T=2s. The performance of the model at varying wave period is given in Table 3.2.

Table 3.2 Performance Parameters at Different Wave Period

Period (s)	Wave Height (m)	P_{Wave} (W/m)	P_{Avail} (W)	P_{WP} (W)	Primary Energy Conversion (C_f)
2	0.14	22.2	19.8	5.9	0.30
2.25	0.155	29.5	26.1	12.1	0.47
2.5	0.23	68.6	60.0	29.9	0.50
2.75	0.18	44.1	38.4	22.6	0.59
3	0.165	38.1	37.0	27.1	0.81

It is apparent from Table 3.2 that at T=2.5s the incoming waves have maximum wave energy flux of 68.6 W/m. At lower wave period of T=2s and T=2.5s there is dramatic decrease in wave power for instance at T=2s the wave power, P_{Wave}=22.2W/m. This is opposite of what was expected since the wave height should have increased with decreasing period. The decrease is due to the fact that the wave height reduces significantly because of wave breaking. The wave power increases from 38.13W/m to 44.1W/m for T=3s to T=2.75s respectively as expected.

Similar trend is since for the water power, the maximum, P_{WP}=29.9W was recorded for T=2.5s. The lowest, P_{WP}=5.9W was recorded at the wave period of 2s. The water power is simply the power in the augmentation channel and it is greatly affected by the wave conditions. As earlier explained at T=2s there is wave breaking and the flow does not have enough energy to funnel through the channel. This leads to lower effective head difference, ΔH across the front nozzle and rear nozzle which also affects the oscillation in the rear chamber. For T=3s, the effective head difference was the highest as well as the oscillation in the rear chamber however, the flow rate is less than that at T=2.5s. This is the sole reason as to why the water power at T=2.5s is more than that at T=3s.

The primary energy conversion, C_f, on the other hand is maximum for T=3s which is 0.81. This means that at wave period of 3s, about 81% of the energy which is available at the front guide nozzle inlet is converted to water power in the augmentation channel. Energy conversion increases with increasing wave period. It is important to take into account the wave power when deciding at which wave period the model performed the best. Even though at T=3s, the maximum energy conversion occurred but at the same time the wave power, P_{Wave}=38.13W/m, was lower than that at T=2.5s.

Therefore, from the study it is clear that at T=2.5s and H=0.23m maximum water power is obtained. The next step forward is to maximize the water power and hence the primary energy conversion by making design changes to the existing base model. The following sections will deal with these issues.

3.5 Front Guide Nozzle Shape

The front guide nozzle guides the flows towards the augmentation channel and its performance also affects the performance of the channel greatly. Since the flow is oscillating, the water constantly flows in and out of the front guide. It must be designed in such as way that there is a gradual increase in the velocity as the water flows from the inlet to the exit of the front guide. In addition to this, the design should be such that it improves the flow characteristics in the attachment down stream to it, mainly the augmentation channel.

The velocity vector at the same time instant when water is flowing in for different front guide nozzle is shown in Fig. 3.15. For Guide 1, 2, 4 and 5 when water enters the guide, a re-circulating region is observed at the upper exit of the front guide nozzle denoted as A. This draws the flow downwards and hence higher velocity is recorded in section labeled B in Fig. 3.15. However, for Guide 3, recirculation is seen near the bottom wall at section B and this diverts the flow upwards.

In Guide 5 the flow converges smoothly at the front guide nozzle exit. Close up view of flow at the guide nozzle exit for Guide 5 is also shown in Fig. 3.15, bottom right. The re-circulating region in Guide 5 is smaller than the rest of the guides studied. Due to this the velocity at the nozzle exit is higher for Guide 5 and hence the flow down stream in the augmentation channel.

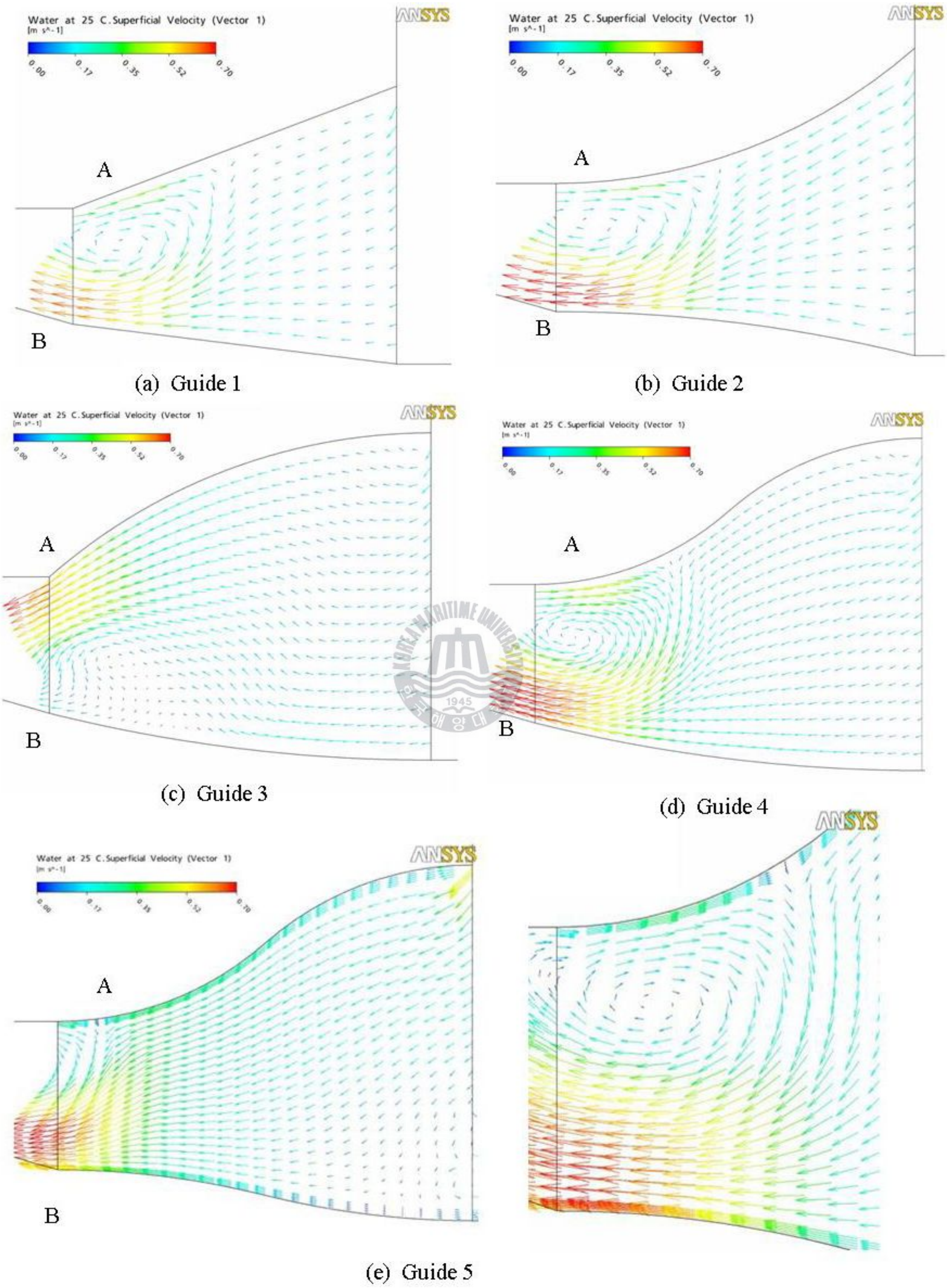

Figure 3.15 Velocity Vector in Different Front Guide Nozzles

The average velocity in the front guide nozzle is shown in Fig. 3.16. $x/L_o=0$ is at front guide nozzle inlet and $x/L_o=1$ is at the exit. L_o is the length of the front guide nozzle which was 700mm. The results show gradual velocity increase in the guide nozzle as desired. The highest velocity is recorded in Guide 5 while the lowest is observed in Guide 3.

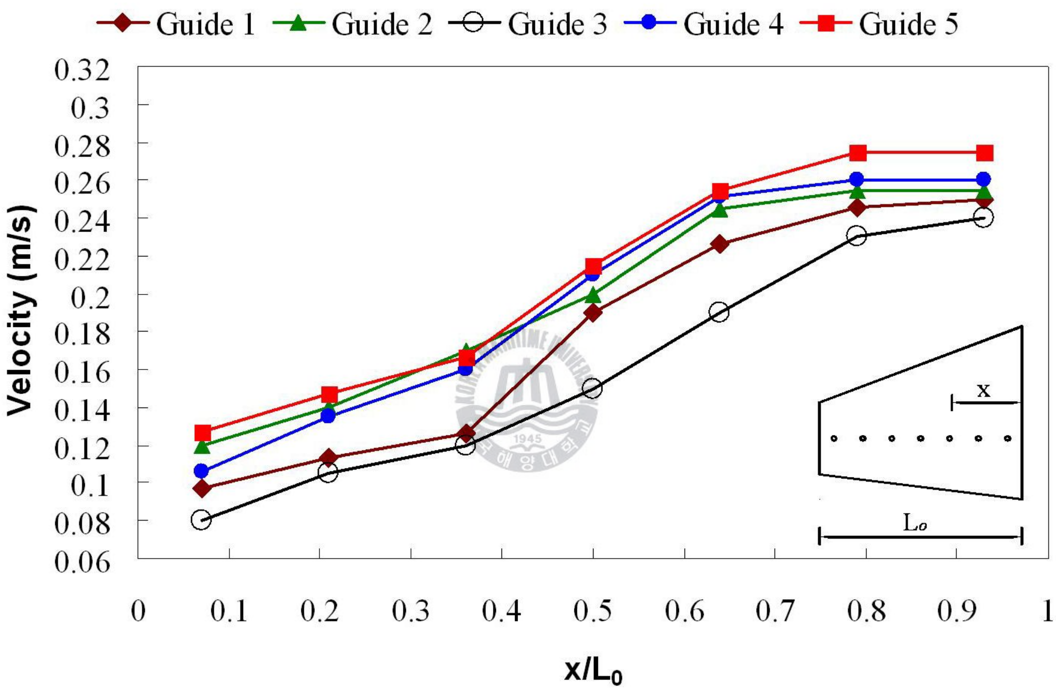

Figure 3.16 Average Velocity for Different Front Guide Nozzles

Figure 3.17 shows the velocity recorded at section 1 to section 3 in the front guide nozzle in the XY plane at $z = 0$. $y/H_{oi}=0$ is the point on the lower wall while $y/H_{oi}=1$ is a point on the upper wall. H_{oi} is the cross sectional height at section i that is at sections 1 to 3. Looking at the velocity at section 1 and 2, velocity recorded near the upper wall is higher than that recorded near the lower wall. For section 1 the velocity changes dramatically from y/H_{oi}=0.35 and for section 2 it occurs at y/H_{oi}=0.25. At front guide nozzle exit, that is at section 3, the velocity near the centre, y/H_{oi}=0.5 is lower than that recorded at the outer walls. There is a sharp decrease which is due to the-recirculation region as described earlier in Fig. 3.15. However, higher velocity is again recorded near the upper wall than the lower wall.

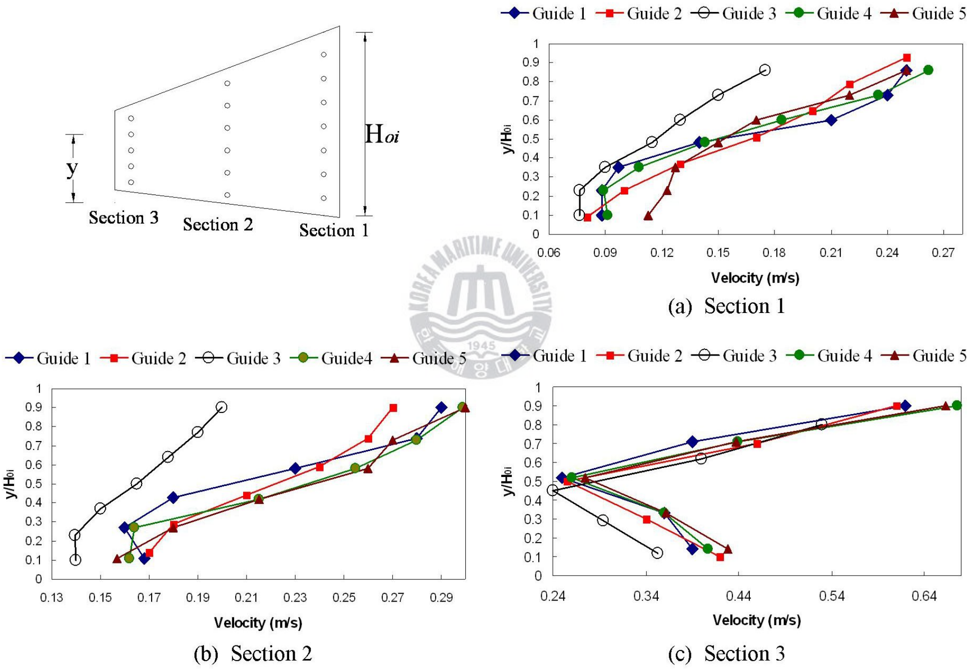

Figure 3.17 Average Velocity for Different Front Guide Nozzles in XY Plane at z = 0

Since the front guide nozzle is symmetric about the x-axis, monitoring points were assigned to half the section as shown in Fig. 3.18. z/W_{oi}=0 is the centre and z/W_{oi}=1 is a point on the side wall. Looking at section 6, higher velocity was recorded near the side walls when compared to the velocity at the centre. At section 5 the velocity drops from the centre but then gradually increases from z/W_{oi}=0.25 onwards to the side wall for Guides 1 to 4 but for Guide 5 there is a slight drop in velocity. However, at section 5 the highest velocity is recorded in Guide 5. At section 4 the variation in velocity from the centre to the side wall is similar to that seen at section 5.

The velocity recorded in Guide 3 was the lowest and the highest was recorded in Guide 5. The velocity increase with respect to the velocity recorded in Guide 1 (base model) for Guide 2, Guide 4 and Guide 5 is 8%, 11% and 15% respectively. On the other hand, in Guide 3 there is an 8% decrease in the velocity. The flow is observed to be better in Guide 5 and hence better performance.

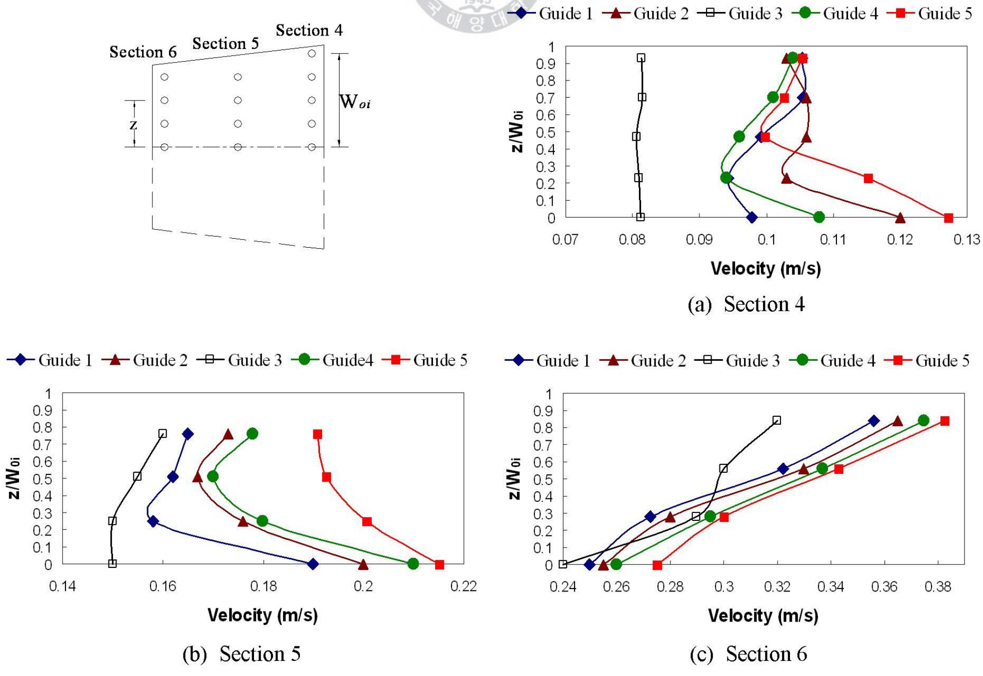

(a) Section 4

(b) Section 5

(c) Section 6

Figure 3.18 Average Velocity for Different Front Guide Nozzles in XZ Plane at y = 0

The effect of front guide nozzle shape on the flow in the augmentation channel more specifically in the front nozzle is shown in Fig. 3.19. It is interesting to see that the velocity recorded at the periphery for Guide 3 model is higher than base model and Guide 2 model. If you refer to figures 3.16 to 3.18 one would see that the velocity in Guide 3 was lower than that recorded in Guide 1 and Guide 2. The results suggest that the flow in the augmentation channel for Guide 3 model is better than that of Guide 1 and Guide 2 models. The highest velocity is recorded for Guide 5; it corresponds to an increase of 7% when compared to base model (Guide 1).

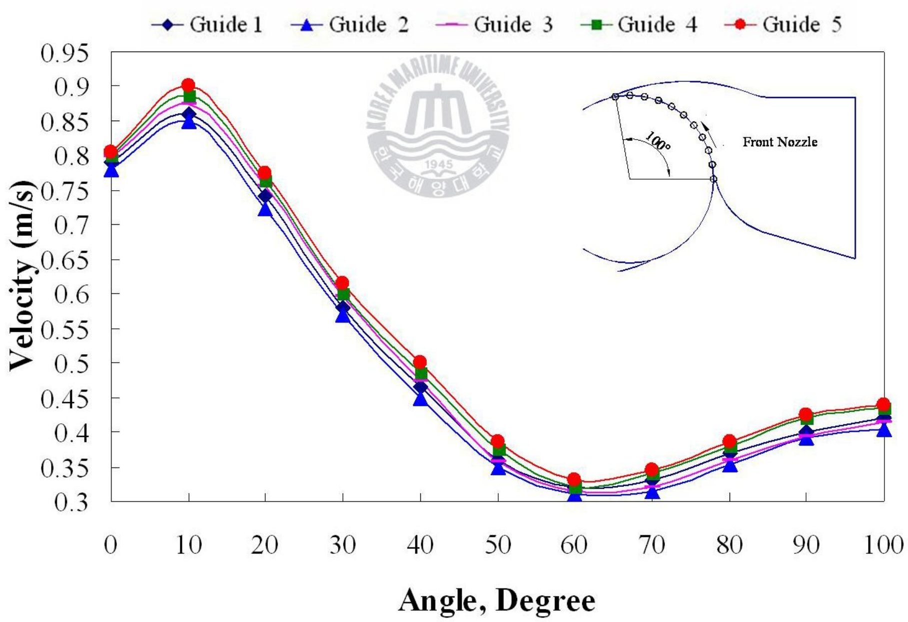

Figure 3.19 Average Velocity at the Periphery for Different Front Guide Nozzles

Using Guide 5, the flow is directed towards the augmentation channel more effectively and the flow is also smooth It could also be said that the losses in Guide 5 is lower than that of the other guide nozzles and this in turn has a positive effect on the flow down stream. For Guide 3 and Guide 4 the velocity recorded at the periphery is 2% and 4% higher than base model. There is a reduction of 2% for Guide 2 when compared with base model (Guide 1)

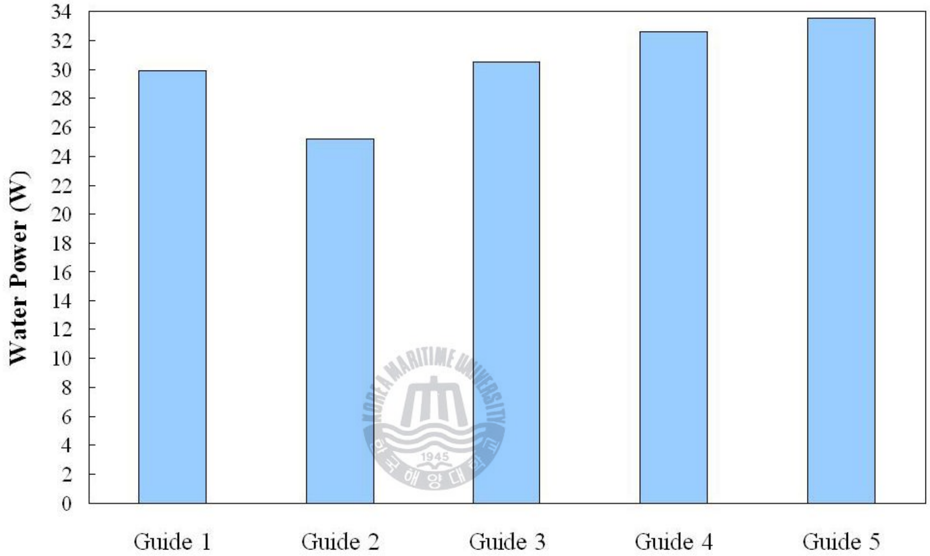

Figure 3.20 Water Power for Different Front Guide Nozzles

The water power, P_{WP} for the five front guide nozzles is given in Fig. 3.20. For the base model (Guide 1) the water power was 29.9 W. The results indicates that the shape of the front guide nozzle influences the water power and hence the primary energy conversion of the system. It is important to highlight that the inlet to outlet area ratio for the guide nozzle was kept constant at 3. Guide 2 recorded the lowest power, P_{WP}=25.2W which is a decrease of 15.7% compared to the base model. For Guide 3 the water power increase was moderate however for Guide 4 and Guide 5 the increase was significant.

For Guide 4, P_{WP}=32.6W and for Guide 5, P_{WP}=33.5W and the corresponding increases were 9% and 12.2% respectively.

Using Guide 5, the primary energy conversion increased from 0.5 for base model to 0.56, which represents an increase of 12%. Given the same wave conditions, the energy conversion is maximum using Guide 5. This increase is a result of better flow characteristics in the front guide as well as down stream in the augmentation channel. The loss is low and hence more energy is available in the augmentation channel which ultimately means more power for the runner.

3.6 Rear Chamber Design

The chamber design greatly influences the flow and the performance of the augmentation channel, more specifically the rear nozzle when water is flowing out. It must be designed to reduce the pressure losses in the rear nozzle as well as minimize flow separation. From the previous section (3.5), the best model was selected, that is Guide 5. Modification to the rear chamber was then carried out. The changes were made to the upper sharp corner and the rear bottom wall of the chamber. Each modification is discussed separately.

3.6.1 Upper Sharp Corner

The upper corner was modified by filleting (rounding) it. The radius denoted as upper radius, R_U was between 0mm to 60mm in increments of 10mm. Case allocation is shown in Table 3.3.

Table 3.3 Case Allocation Upper Sharp Corner Modification

Upper Radius, R_U(mm)	Case
0 (Guide 5)	1
10	2
20	3
30	4
40	5
50	6
60	7

The velocity vector in the rear chamber when water is entering the chamber for case 1, 3, 5 and 7 is shown in Fig. 3.21. There is severe flow separation at the upper corner for Case 1 (R_U=0mm) but the separation eases as the fillet radius increases The flow almost follows the wall for Case 5 (R_U=40mm) and Case 7 (R_U=60mm).

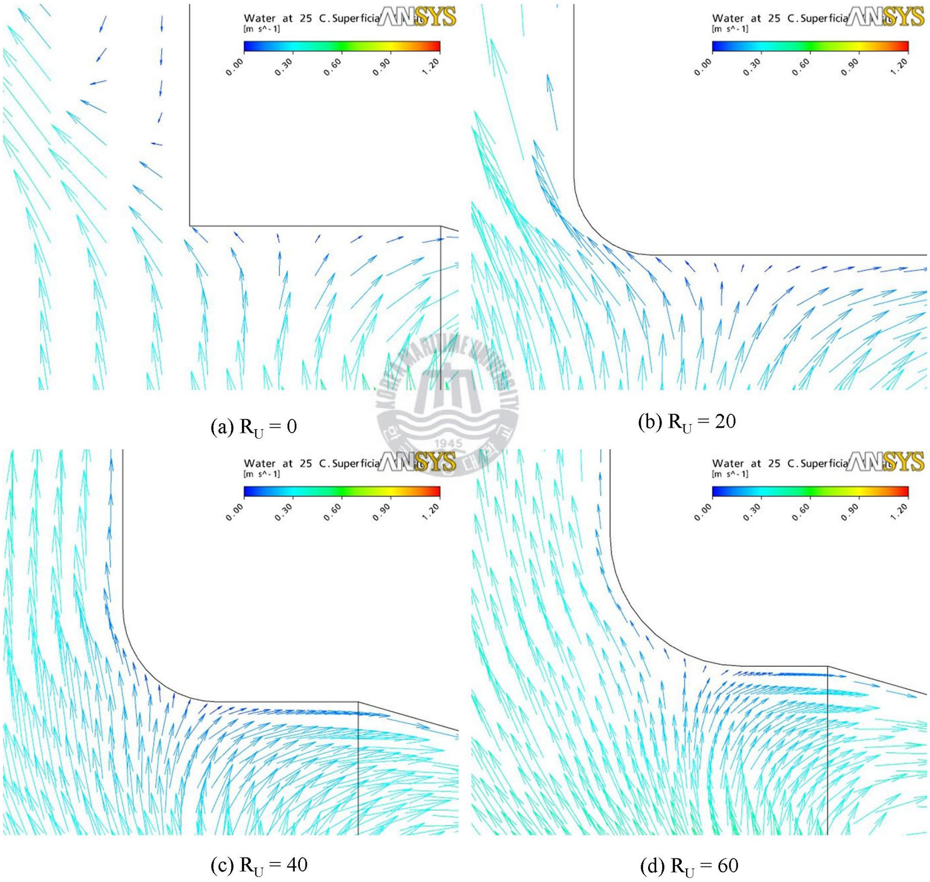

Figure 3.21 Velocity Vector in the Rear Chamber for Different Upper Radius

The velocity vector in the rear chamber for case 1 and 5 is shown in Fig. 3.22. The vector is drawn for the same time instant and shown when water is entering the chamber and flowing out of it. It is clear that higher velocity is recorded when water is entering for Case 5 (R_U=40mm) which leads to higher oscillation in the chamber hence there is more energy available when water falls and flows out of the chamber. The effect of making the upper corner into a fillet is more profound when water is following out. For Case 1 (R_U=0mm) there is a wider region of re-circulating flow when water is flowing out than compared to Case 5 (R_U=40mm) as shown in Fig. 3.22. For Case 5 (R_U=40mm) higher velocity is observed near the upper wall when water is following of the rear chamber hence better flow in the rear nozzle.

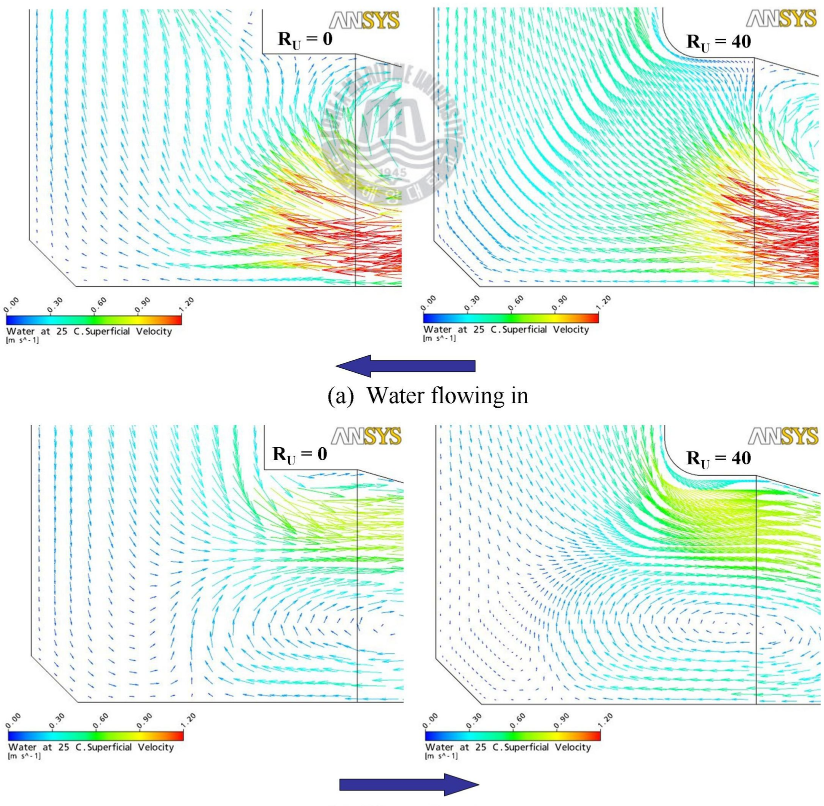

(a) Water flowing in

(b) Water flowing out

Figure 3.22 Velocity Vector in the Rear Chamber for Case 1 and Case 5

Figure 3.23 shows the total pressure for Case 1 and Case 5. The total pressure recorded in the front nozzle for both the cases does not vary much but there is a significant change in the total pressure recorded in the rear nozzle. Due to this change, there is a considerable difference in the effective head across the front nozzle and rear nozzle as shown in Fig. 3.24.

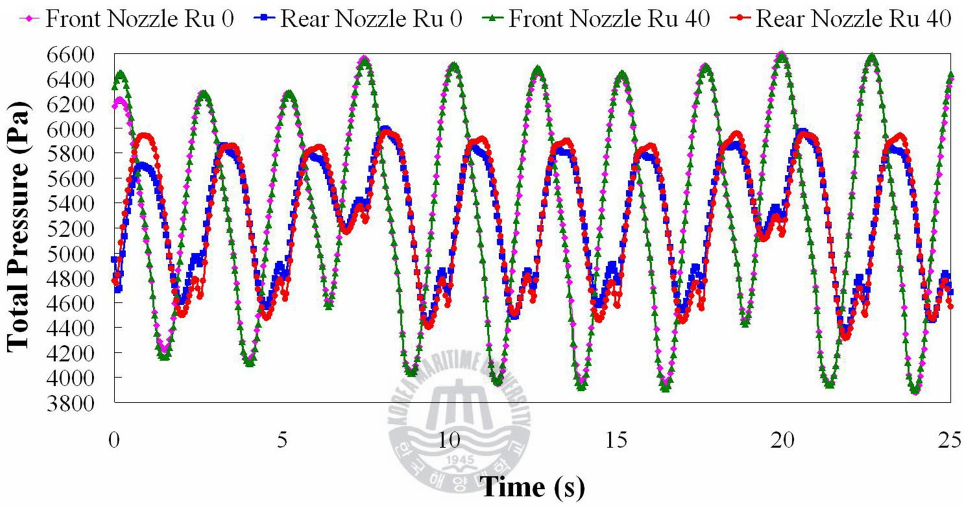

Figure 3.23 Total Pressure in the Front Nozzle and Rear Nozzle for Case 1 and Case 5

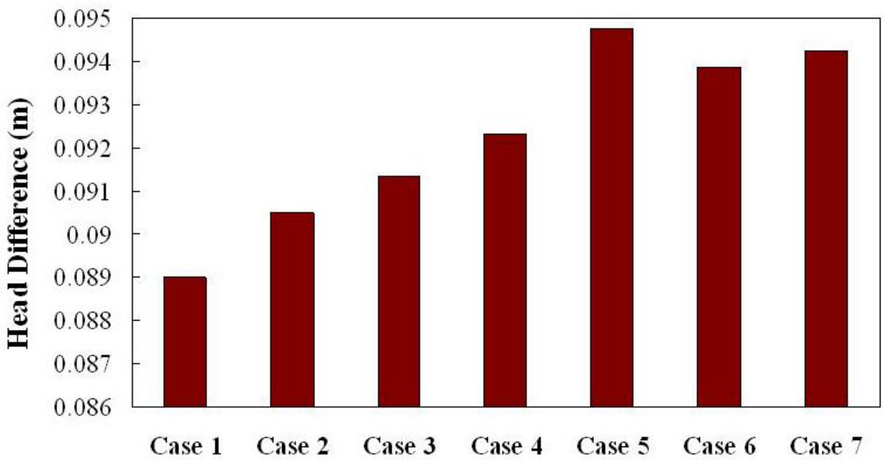

Figure 3.24 Effective Head Difference Across Front Nozzle and Rear Nozzle

The changes made to the rear chamber also affects the flow upstream for instance in the front guide nozzle and the front nozzle (periphery). The average velocity recorded in the front guide nozzle for case 1, 3, 5 and 7 is shown in Fig. 3.25 There is a slight increase in the velocity as the radius increases when compared to the Case 1 (R_U=0mm). However, the velocity is maximum in Case 5 (R_U=40mm). The overall increase in velocity in the front guide nozzle of Case 5 compared to Case 1 is approximately 4.9%.

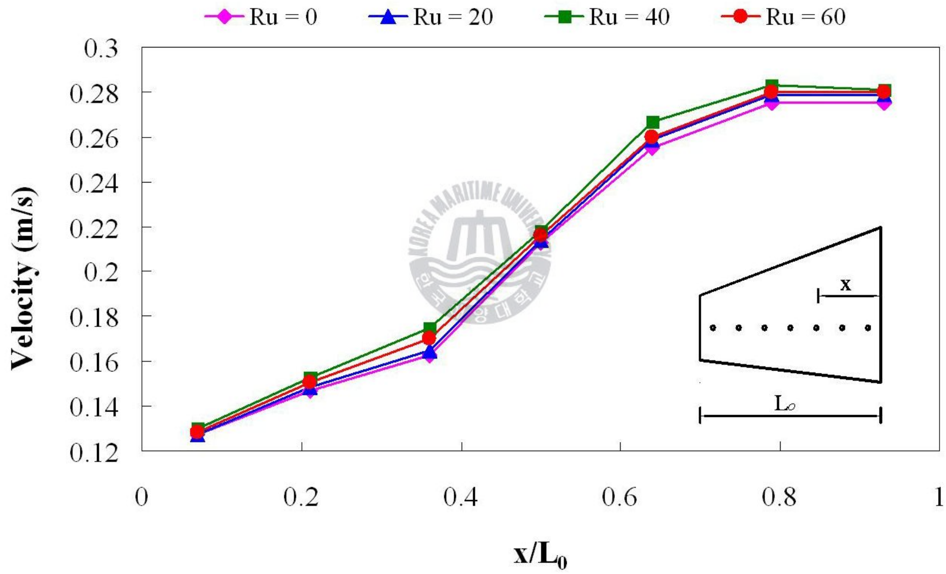

Figure 3.25 Average Velocity in the Front Guide Nozzle for Different Rear Chamber Upper Radius

Table 3.4 highlights the water power and the primary energy conversion for cases 1 to 7 and it also includes the base model. The results indicate that by making the sharp corner smooth the water power and hence the energy conversion could be increased. Water power increases as the fillet radius increases and at R_U=40mm (Case 5) maximum power of 37.1W is obtained. Any increase beyond this does not increase or improve the energy conversion further.

The increase in the water power and primary energy conversion for Case 5 with respect to Case 1 was 11%. The increase is substantial and shows that by making changes to the rear chamber a favorable flow in the front guide nozzle, augmentation channel and in the rear chamber can be achieved. The performance of Case 5 with respect to the base model (Guide 1) shows an increase of 24% in the water power and first stage energy conversion.

Table 3.4 Water Power and Energy Conversion Comparison

Case	Water Power P_{WP}(W)	Primary Energy Conversion (C_f)
Base Model (Guide 1)	29.9	0.50
1 (Guide 5)	33.5	0.56
2	34.1	0.57
3	34.8	0.58
4	35.4	0.59
5	37.1	0.62
6	36.0	0.60
7	36.2	0.60

3.6.2 Rear Bottom Wall

Taking Case 5 (R_U=40mm) from section 3.6.1, further design changes are made to the chamber that is; the rear bottom wall. The rear bottom wall was modified in similar fashion as the upper sharp corner. The lower radius, R_L, ranged from 40mm to 160mm in increments of 40mm. Case allocation and the corresponding water power is given in Table 3.5. The velocity recorded at the periphery for Case 5 and Case 8 to 11 is shown in Fig. 3.26. Case 8 to 11 recorded lower velocity than Case 5. The lowest velocity was recorded for R_L=40mm and for R_L= 40, 120 and 160mm; the velocity was almost the same. It is clear that all the latter models recorded lower velocity than Case 5.

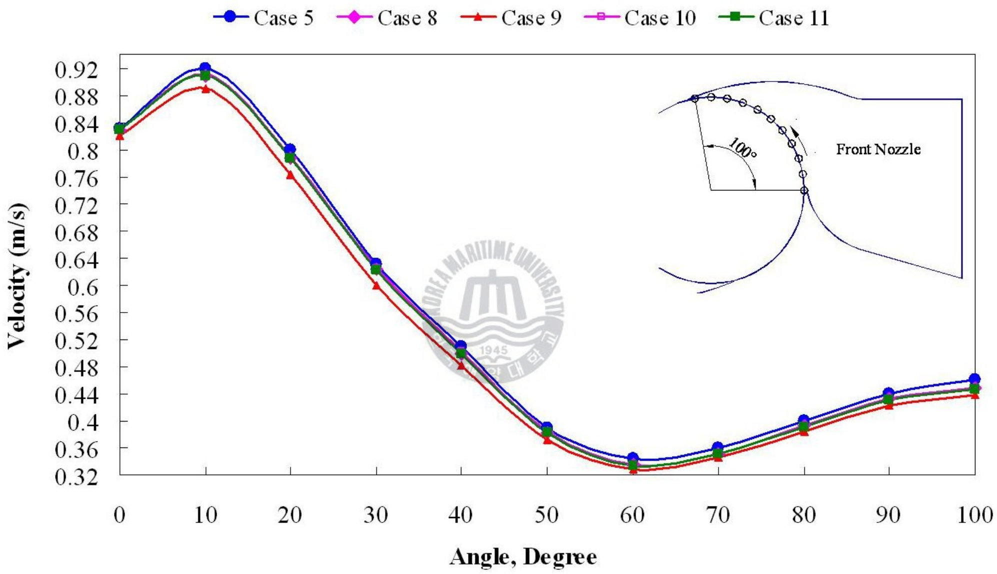

Figure 3.26 Average Velocity at the Periphery for Different Rear Bottom Wall Radius

It was observed that the water power decreases appreciably when compared to Case 5. For Case 8 to Case 11, making the rear bottom wall round has little or no effect on primary energy conversion. The power is almost constant through out. Therefore, it can be concluded from this section that after making the desired changes, of all the configurations tried, Case 5, which consist of Guide 5 and rear chamber design with R_U=40mm and R_L=0mm performed the best.

Table 3.5 Case Allocation and Water Power for Rear Bottom Wall Modification

Lower Radius, R_L(mm)	Case	Water Power P_{WP} (W)
0 [Case 5 (R_U=40mm)]	5	37.10
40	8	34.46
80	9	34.27
120	10	34.62
160	11	34.62

3.7 Augmentation Channel Geometry

The flow in the augmentation channel is really important as it directly interacts with the runner, hence its design must be such that the losses are minimized at the same time the flow characteristics should be favorable. Four additional augmentation channel geometries were studied and modification was made to the base model. Table 3.6 shows the details and also refer to section 2.3.2 of methodology section. Note that the front guide nozzle and the rear chamber used are the original ones (base model). The purpose of this study is to observe how the entrance arc, the rear spiral wall radius (shape) affects the flow characteristics mainly in the augmentation channel and the primary energy conversion.

Table 3.6 Different Augmentation Channel Geometries

Augmentation Channel Geometry	**Model**	**Entrance Arc, E_A (°)**	**Rear Spiral Wall Radius**
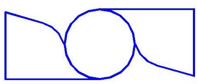	Straight Wall **[ST]**	90	-
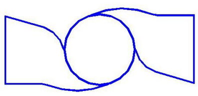	Spiral Wall 1 (Base Model) **[SP 1]**	105	290
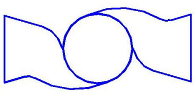	Spiral Wall 2 **[SP 2]**	105	290
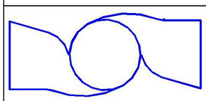	Spiral Wall 3 **[SP 3]**	125	290
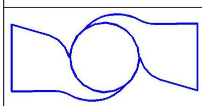	Spiral Wall 4 **[SP 4]**	125	Logarithmical Spiral

The velocity vector when water is flowing into the augmentation channel at the same time instant is shown in Fig. 3.27. When water is advancing re-circulating flow is observed in regions A and B while when water is flowing out of the augmentation channel vortices are observed in regions C and D as shown for Spiral Wall 1 in Fig. 3.27. From the figure below, for Spiral Wall 4 model, there is an increase in the velocity. This increase is due to better flow characteristics in the augmentation channel.

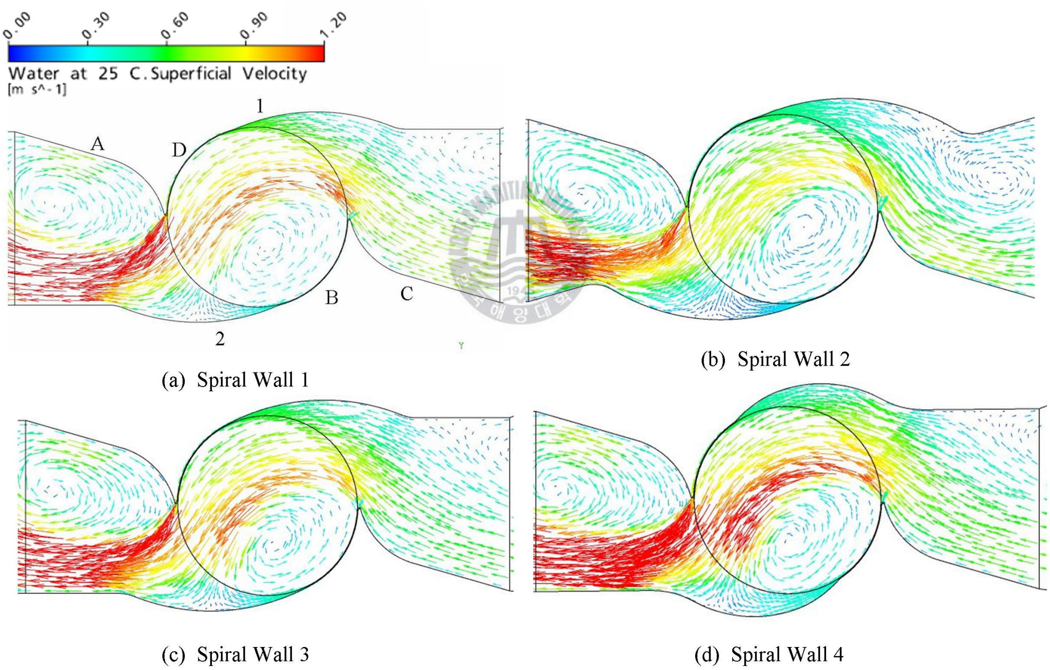

Figure 3.27 Velocity Vector in Different Augmentation Channel Geometries

The velocity vector at the rear wall is shown in Fig. 3.28. For the straight wall model, when water enters the channel, the fluid near the top wall of the front nozzle right before the internal fluid region seemed to collide with the upper wall (region 1) as shown in Fig. 3.28 (top right). This results in the severe flow modification and thus leads to lower velocity and hence inferior performance. For the spiral rear wall models; having the rear wall spiral ensures that the fluid enters smoothly and with uniform acceleration which results in better flow as shown in Fig. 3.28. It is clear from the flow pattern as highlighted by the vectors that for Spiral Wall 4 the water is guided more smoothly. The result is apparent when comparing it with Straight Wall model just by looking at the curvature of the flow.

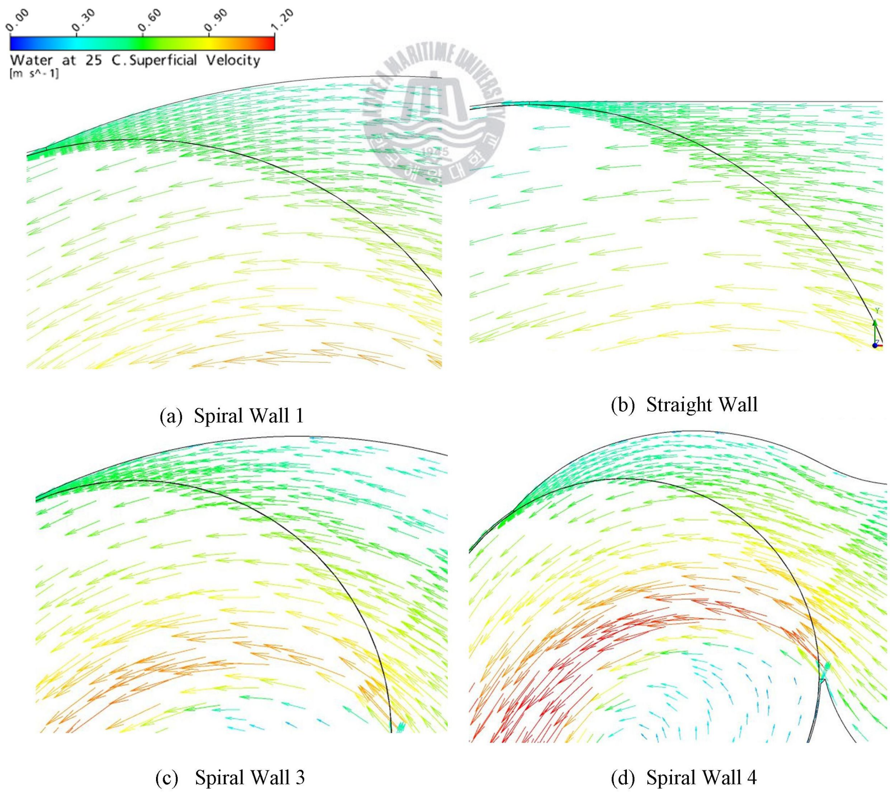

(a) Spiral Wall 1 (b) Straight Wall

(c) Spiral Wall 3 (d) Spiral Wall 4

Figure 3.28 Velocity Vector at the Rear Wall

The result of the vector flow in the augmentation channel is quantified in Fig. 3.29 which shows the average velocity recorded at the periphery for the 5 models. All the spiral wall models performed better than the Straight Wall which validates early statement. On the other hand, Spiral Wall 2 recorded lower velocity, a decrease of about 3% than the base model (Spiral Wall 1). To investigate the effect of entrance arc, base model was compared with Spiral Wall 3. The results indicate by making the entrance arc larger, the flow rate increases as well as there is increase of approximately 3% in the velocity recorded at the periphery.

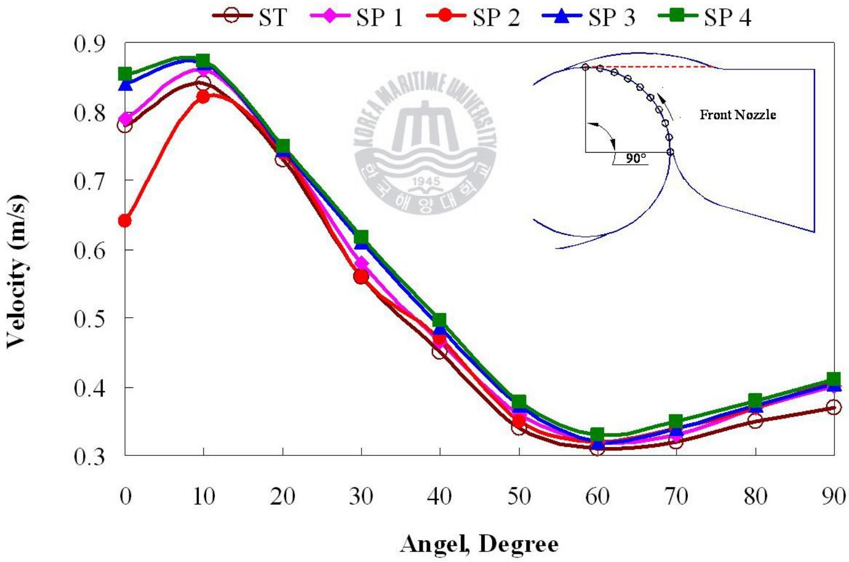

Figure 3.29 Average Velocity at the Periphery for Different Augmentation Channel Geometries

For effect of the rear wall spiral on flow characteristics, Spiral Wall 4 and Spiral Wall 3 models were compared. By making the rear wall more spiral, the flow characteristics could be improved in the augmentation channel as shown Fig. 3.28.

For Spiral Wall 4 the velocity at the periphery is slightly higher than Spiral Wall 3 model. There is a 5% increase in the average velocity recorded at the periphery for Spiral Wall 4 when compared to the base model (Spiral Wall 1). Figure 3.30 shows the total pressure in the front nozzle and the rear nozzle for Spiral Wall 4 and Spiral Wall 1 (base model). Higher pressure is observed for Spiral Wall 4 in both the front nozzle and rear nozzle which increase the effective head.

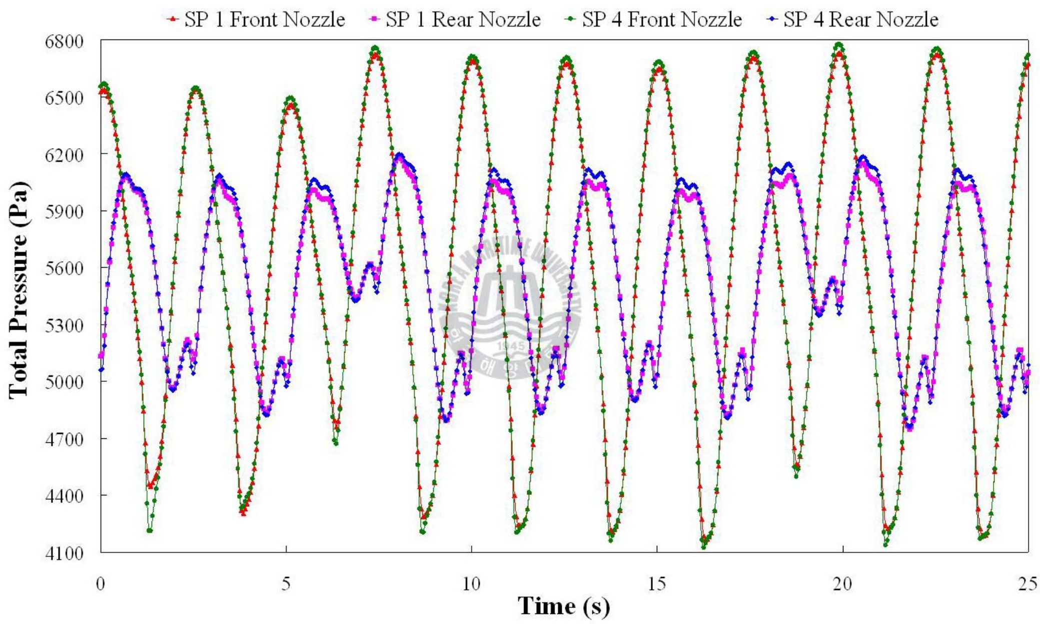

Figure 3.30 Total Pressure in the Front Nozzle and Rear Nozzle for Spiral Wall 1 and Spiral Wall 4

The geometry of the augmentation channel also affects the flow up stream in the front guide nozzle. The average velocity recorded at points 1 to 4 is given in Fig. 3.31. There is an increase of 8% in the velocity recorded in the front guide nozzle for Spiral Wall 4 compared to base model (Spiral Wall 1).

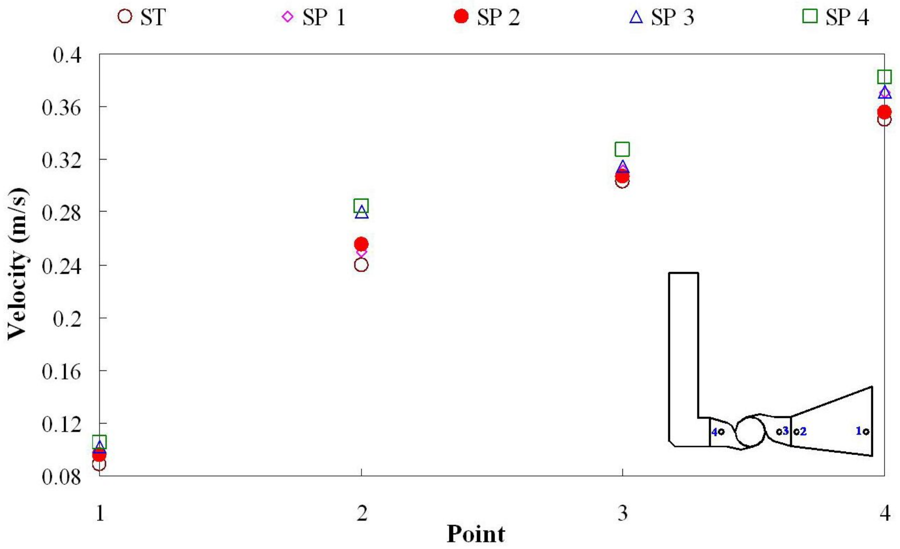

Figure 3.31 Average Velocity at Points 1 to 4 for Different Augmentation Channel Geometries

Table 3.7 Performance Parameters for Different Augmentation Channel

Model	Flow rate (m^3/s)	Water Power P_{WP} (W)	Primary Energy Conversion (C_f)
Straight Wall	0.0339	27.2	0.45
Spiral Wall 1 (Base Model)	0.0364	29.9	0.50
Spiral Wall 2	0.0353	28.66	0.48
Spiral Wall 3	0.0366	31.17	0.52
Spiral Wall 4	0.0371	32.57	0.54

Table 3.7 shows the performance parameters for the 5 different augmentation channels. The water power for Straight Wall and Spiral Wall 2 model is lower than the base model. The decrease is 9% and 4% respectively. Maximum water power of 32.57W was achieved using Spiral Wall 4

augmentation channel. There is an increase of 4% and 9% in the water power for Spiral Wall 3 and Spiral Wall 4 respectively with respect to the Spiral Wall 1(base model). The base model and Spiral Wall 3 have the same rear spiral radius and just by changing the entrance arc length the water power increased from 29.9W to 31.17W for the latter model. The flow rate increased slightly however, there was an increase in the head difference across the front and rear nozzle for Spiral Wall 3.

Keeping the entrance arc, E_A same at 125° the effect of rear spiral wall on water power and primary energy conversion was investigated by comparing Spiral Wall 3 and Spiral Wall 4. Higher energy conversion is obtained by making the rear wall more spiral and this is evident from Table 3.7. Spiral Wall 4 recorded P_{WP}=32.57W which corresponds to an energy conversion of 0.54 which was 4% higher than Spiral Wall 3.

Finally, the design change suggests that the best geometry for the augmentation channel is Spiral Wall 4. The overall performance with respect to the base model (Spiral Wall 1) shows an increase of 8% in the primary energy conversion. So under same wave conditions, using Spiral Wall 4, higher power can be achieved. This increase is due to increase in the flow rate as well as better flow characteristics in the augmentation channel as well as the flow upstream in the front guide.

3.8 Final Model Simulation

After making changes to the front guide nozzle, the augmentation channel and the rear chamber; the best design from each modification was integrated and the final model was obtained. Table 3.8 summarizes the optimization process to obtain the best model configuration. Figure 3.32 shows the final model configuration compared with the base model.

Table 3.8 Final Model Details

PART	Specification	Results Section	Model
Front Guide Nozzle	Guide 5	3.5	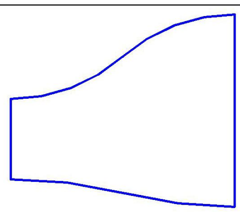
Rear Chamber	Case 5 **[R_U = 40 mm]** **[R_L = 0 mm]**	3.6.1	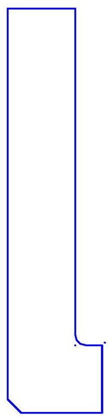
Augmentation Channel	Spiral Wall 4 **[SP 4]**	3.7	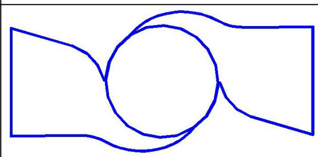

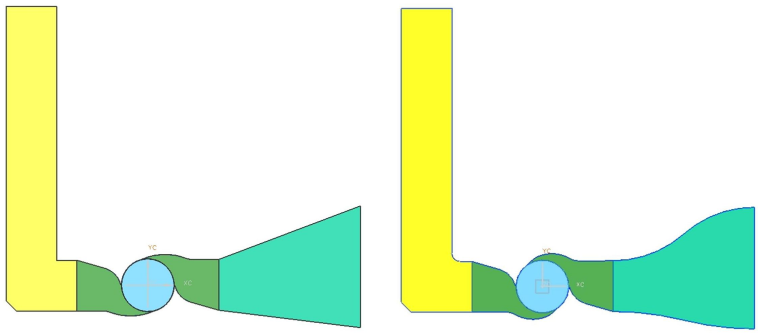

(a) Base Model (b) Final Model

Figure 3.32 Base Model and Final Model Configuration

Table 3.9 Velocity Vector in the Base Model and the Final Model

Base Model	**Final Model**
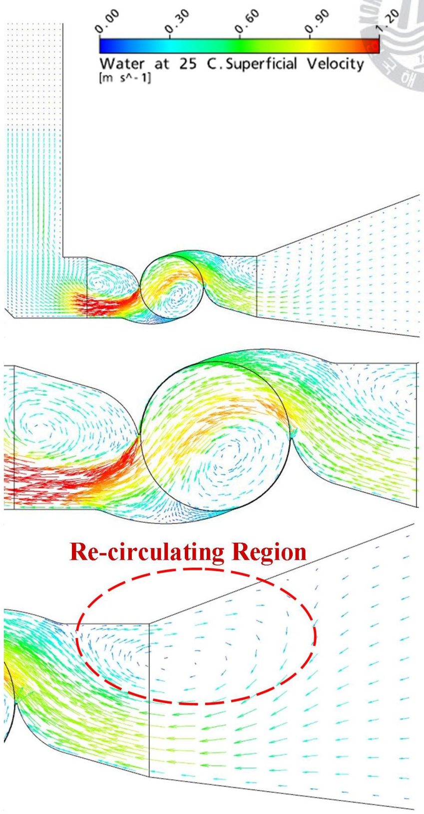	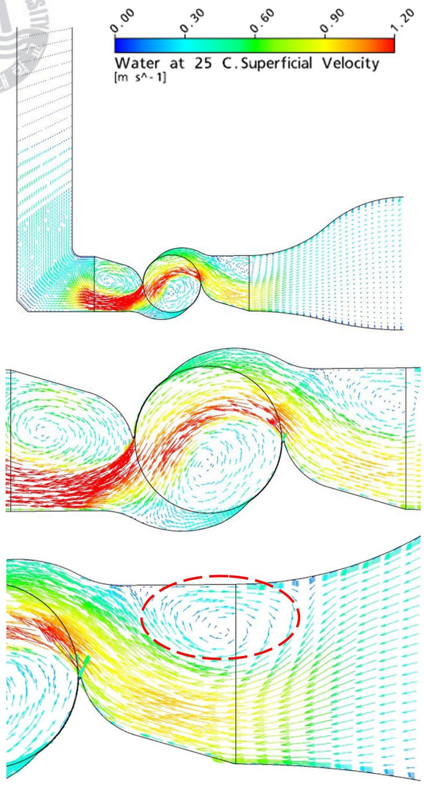

Velocity vector in the base model and final model is given in Table 3.9. The vectors are drawn when the water is entering the channel. It is very clear from the vectors that higher velocity is recorded in the best model configuration. In addition to this, the re-circulating flow region grows smaller in size for the final model in comparison to the base model and this is the reason for higher flow velocity recorded in the final model.

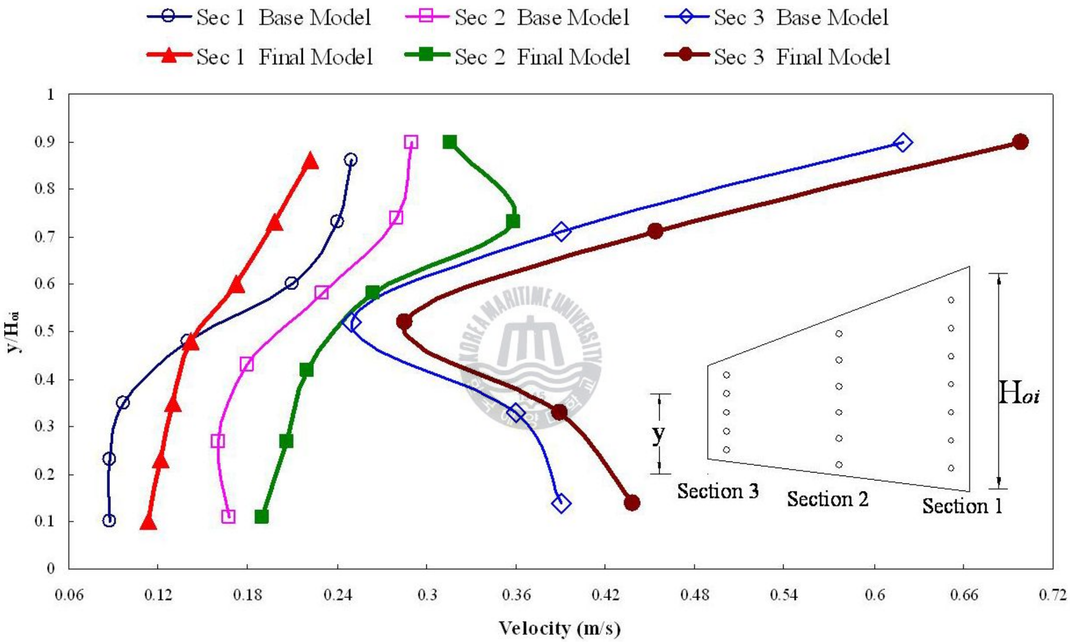

Figure 3.33 Average Velocity in XY Plane at z = 0 in the Front Guide Nozzle for Base Model and Final Model

Figure 3.33 shows the velocity in the XY plane at z = 0. The velocity recorded at section 2 and section 3 in the front guide nozzle of the final model is considerably higher than that of the base model. However, at section 1 from $y/H_{oi}=0.5$, the velocity recorded at the upper wall section is higher for the base model.

The velocity in the XZ plane at y = 0 in the front guide nozzle of base model and the final model is given in Fig. 3.34. The velocity is higher in the front guide nozzle of the final model at all the sections (sections 4 to 6). The overall velocity increase compared to the base model is about 16%.

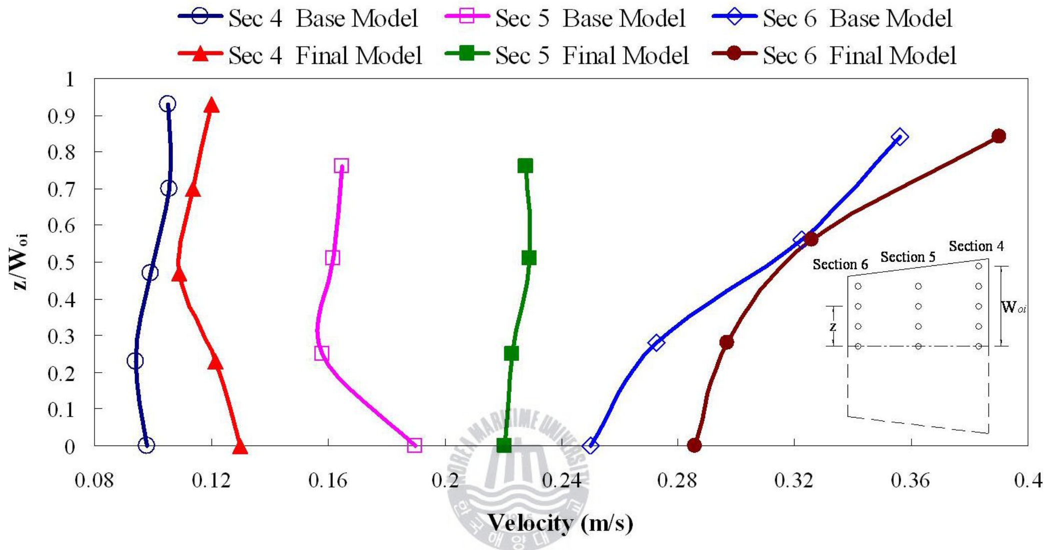

Figure 3.34 Average Velocity in XZ Plane at y = 0 in the Front Guide Nozzle for Base Model and Final Model

Table 3.10 Performance Parameter for the Base Model and Final Model

Parameter	Base Model	Final Model
ΔY (m)	0.26	0.29
Q (m^3/s)	0.0364	0.0406
ΔH (m)	0.084	0.101
Water Power, P_{WP} (W)	29.9	40.2
Primary Energy Conversion, C_f	0.50	0.67

Performance parameters for the base model and final model are given in Table 3.10. The main focus is on water power and the energy conversion. By undertaking design optimization of the various parts, the outcome is the final model. For the final model the water power or the power available in the augmentation channel was 40.2W which is an increase of 34% compared to the base model.

Just by making changes to the base model the primary energy conversion is increased from 0.50 to 0.67 under same wave conditions. The final model configuration is able to convert 67% of the power available at the front guide nozzle inlet to water power available in the augmentation channel.

The overall optimization yields better flow characteristics in the front guide nozzle, the augmentation channel and in the rear chamber of the final model. As mentioned earlier the velocity in the front guide nozzle of the final model is 16% higher than the base model and also an increase of 10% is recorded for the peripheral velocity. This improvement thus leads to higher energy conversion.

CHAPTER 4 CONCLUSION

The effect of front guide nozzle divergent angle, front guide nozzle shape, augmentation channel geometry and rear chamber design on flow, the water power and primary energy conversion was successfully investigated in this study.

From the present study the following observations were made:

- There is an increase of 19% in the water power for the model with front guide nozzle divergence angle of α=14°. However, the primary energy conversion remains the same for both α=0° and α=14° models.

- The maximum power in waves, P_{Wave}=68.6W/m is obtained at wave period of T=2.5s and wave height of H=0.23m. At lower wave periods there is wave breaking which results in lower power in the incoming waves.

- Amongst the various front guide nozzle shapes tested, Guide 5 performed the best. Not only was the flow characteristic better in the front guide but also down stream in the augmentation channel. The increases in the average velocity recorded in the guide nozzle and at periphery in the augmentation channel were 15% and 7% respectively when compared to the base model. The resulting increase in primary energy conversion with respect to the base model (Guide 1) was 12%.

- The rear chamber design influences the power available in the augmentation channel greatly. The best chamber design was the one with upper radius, R_U=40 mm and lower radius, R_L=0mm (Case 5). Water power for this model was 37.1W which corresponds to an increase of 24% in the water power and the primary energy conversion compared to the base model. With respect to Guide 5 (Case 1) model the increase in energy conversion was 11%. Modifying the rear bottom wall of the chamber reduces the energy conversion.

- From the five augmentation channel geometries tested, Spiral Wall 4 recorded the highest water power of 32.57W. This represents an increase of 8% in the primary energy conversion compared to the base model (Spiral Wall 1). The rear spiral wall of this model helps to guide the flow more smoothly and with uniform acceleration.

- After obtaining the best designs of all the individual components, a final model was obtained and its performance with respect to the base mode was investigated. The water power and the primary energy conversion for the final model were 40.2W and 0.67 respectively. It is an increase of 34% compared to the base model.

Finally, the overall results show that by making design changes to front guide nozzle, augmentation channel and the rear chamber the water power and hence the primary energy conversion of the system can be improved under same wave conditions.

ACKNOWLEDGEMENT

Foremost, I would like to express my sincere gratitude to my supervisor Prof. Dr. Young-Ho LEE for the continuous support of my Master's study and research, for his patience, motivation, enthusiasm, and immense knowledge in the field of wave power extraction and fluid dynamics. His guidance helped me a lot during the duration of my research. I could not have imagined having a better supervisor and mentor for my Master's study.

Besides my supervisor, I would like to thank the rest of the thesis committee: Prof. Dr. You-Taek KIM (Chairperson) and Prof. Dr. Kweon-Ha PARK (Co-Chairperson) for their encouragement, helpful comments and suggestions.

At this point I would like to thank and show my appreciation for been given a chance to study at Korea Maritime University and pursue my masters degree.

I am indebted to my Korean lab mates who have helped me in translating Korean to English and for their assistance. I would also like to thank my colleague Mr. Mohammed Asid Zullah for his comments and help with ANSYS-CFX software.

Many thanks goes out to my sisters and brother-in-laws who always have been there for me.

Finally, I am heartily thankful for the support and encouragement that my parents have given me in pursuing a Master's degree. I dedicate this thesis to my loving parents.

REFERENCE

[1] Twidell, J. and Weir, T., “Renewable Energy Sources”. E. & F. N. Spon, 29 West 35th Street, New York NY 10001, USA.

[2] Panicker, N. N., “Power Resource Potential of Ocean Surface Waves”. In: Proceedings of the wave and salinity gradient workshop, Newark, Delaware, USA. 1976. pp. J1-J48.

[3] Wavemill Energy Corp., “Electric Power from Ocean Waves”. Online, http://www.wavemill.com. 2010.

[4] Thomas, W. T., “An Overview of Wave Energy Technology: Status, Performance and Costs”. In: Proceedings of a Conference on Wave Power: Moving towards Commercial Viability, Institute of Mechanical Engineers, London, United Kingdom. 1999.

[5] Rodrigues, L., “Wave Power Conversion Systems for Electrical Energy Production”, Department of Electrical Engineering, Faculty of Science and Technology, Nova University of Lisbon, Portugal.

[6] “Wave Energy and Physics and Resource”, Online, http://www.thew2o.net/events/oceanenergy/images/wave_energy.pdf. 2010.

[7] Holthuijsen, L. H., "Waves in Oceanic and Coastal Waters". Cambridge Univ. Press, United Kingdom. 2007.

[8] "Introductory Oceanography - General Ocean Waves Characteristics", Online, http://www4.ncsu.edu/eos/users/c/ceknowle/public/chapter10/part1.html. 2010.

[9] Falnes, J., "A Review of Wave-Energy Extraction". Marine Structures 2007; (20): pp. 185-201.

[10] Stahl, A., "The Utilization of the Power of Ocean Waves". Trans Am. Soc. Mech. Eng., 1892;(13): pp. 438-506.

[11] Leishman, J. M., Scobie, G., "The Development of Wave Power-A Techno-economic Study". East Kilbride, Scotland, National Engineering Laboratory; 1976.

[12] McCormick, M. E., "Ocean Wave Energy Conversion". Wiley, New York. 1981.

[13] Shaw, R., "Wave Energy-A Design Challenge". Ellis Horwood Ltd, Chichester, England. 1982.

[14] Engineering Committee on Oceanic Resources Working Group on Wave Energy Conversion, "Wave Energy Conversion". Elsevier Science Ltd, 2003.

[15] Falnes, J. and Budal, K., “Wave Power Conversion by Point Absorbers”. Norwegian Maritime Res. 1978; 6(4): pp. 2–11.

[16] Falnes, J., “Optimum Control of Oscillation of Wave-Energy Converters”. Int. J. Offshore Polar Eng., 2002; 12 (2): pp.147–55.

[17] Isaacs, J. D., Castel, D. and Wick, G. L., “Utilization of the Energy in Ocean Waves”. Ocean Eng., 1976; (3): pp. 175-187.

[18] Masuda, Y., “An Experience of Wave Power Generator Through Tests and Improvement”. In: Proceedings of IUTAM Symp. On Hydrodynamics of Wave Energy Devices, Springer Verlag, Berlin. 1985.

[19] Salter, S. H., “World Progress in Wave Energy-1988”. Int, J, Ambient Energy, 1989; (10): pp. 3–24.

[20] Salter, S. H., “Wave Power”. Nature 1974; (249): pp. 720–724.

[21] Budal, K. and Falnes, J., “Optimum Operation of Improved Wave-Power Converter”. Mar. Sci .Commun., 1977; (3): pp. 133 –150.

[22] McCormick, M. E., “Analysis of a Wave-Energy Conversion Buoy”. J. Hydronautics, 1974; 8(3): pp. 77-82.

[23] Ross, D., “Power from the Waves”. Oxford University Press, Oxford. 1995.

[24] Bedard, R., “Power and Energy from the Ocean Energy Waves and Tides-A review”. Electric Power Research Institute, 2007.

[25] Global Warming, “Finavera Aquabuoy”. Online, http://www.global-greenhouse-warming.com/Finavera-aquabuoy.html, 2010.

[26] Continental, “Endless Energy: Electric Power from the Ocean”, Online, http://www.contionline.com/generator/www/com/en/continental/pressportal/themes/press_releases/1_topics/conticompact/ms_2008_11_03_en.html. 2010.

[27] Raunekk, Wave Power : Archimedes Wave Swing. Lamar Stonecypher, Online, http/www.brighthub.com/engineering/mechanical/articles/40548.aspx,nline, http:/ 2010.

[28] “Wave Power in Canada,HydrodynamicSystems”. Online, http://www.ccbda.org/electrical_wave_power/electrical_wave_powerS4.htm, 2010.

[29] Partners for Renewables-A Carbon Trust Enterprise,“Oscillating Water Column”. Online, http://www.pfr.co.uk/pfr/page/345, 2010.

[30] Voith Hydro Wavegen Limited, “LIMPET”. Online, http://www.wavegen.co.uk/what_we_offer_limpet.htm, 2010.

[31] “Wave Power”, Online, http://www.esru.strath.ac.uk/EandE/Web_sites/0102/RE_info/wave%20power.htm. 2010.

[32] “Wave Energy Research and Development at JAMSTEC - Offshore Floating Wave Energy Device Mighty Whale”. Online, http://www.jamstec.go.jp/jamstec/MTD/Whale/mwweb1.html, 2010.

[33] “Wave Dragon for Better Future:”. Online, http://www.wavedragon.net, 2010.

[34] “Wave Dragon - den Drachen schwimmem lassen”, Online, http://www.ipp.mpg.de/ippcms/ep/ausgaben/ep200302/bilder/0203_wavedragon2_dia.html. 2010.

[35] Union of Concerned Scientists,“How Hydrokinetic Energy Works”.Online, http://www.ucsusa.org/clean_energy/technology_and_impacts/energy_technologies/how-hydrokinetic-energy-works.html, 2010.

[36] Pelamis Wave Power, ‘The Pelamis Wave Energy Converter”. Online, http://www.pelamiswave.com/content.php?id=161, 2010.

[37] “Wave Energy Potential on the U.S. Outer Continental Shelf”. Minerals Managemen Service, Renewable Energy and Alternative Use Program, U.S. Department of the Interior. 2006.

[38] Wind Propect, “Service and Consultancy”, Online, http://www.windprospect.com.au/technologies?t=wave_pelamis. 2010.

[39] UNENERGY, “Wave, Tidal, River and Hydro Eletricity”, Online, http://www.unenergy.org/index.php?p=1_49_Wave-Power. 2010.

[40] Fukutomi, J. and Nakase, Y,. “A Study of Turbine for Wave Power Generation”. In: Proceedings of the 1st Pacific/Asia Offshore Mechanics Symposium, Seoul, South Korea. 1990; pp. 193-198.

[41] Choi, Y. D., Kim, C. G., Cho, Y. J., Kim, Y. T. and Lee, Y. H., “Internal Flow Characteristics of Cross Flow Hydraulic Turbine for Wave Power System”. In: Proceedings of the 9th AICFM, Jeju, South Korea, 2007; CD-ROM PaperNo:AICFM9-296.

[42] Choi, Y. D., Kim, C. G., Kim, Y. T. and Lee, Y. H., "A Study on the Nozzle Shape of a Cross-Flow Type Hydro Turbine for Wave Power Generation". J. of Fluid Machinery (In Korean), 2008; 11(3): pp. 30-35.

[43] Olgun, H., "Investigation of the Performance of a Cross Flow Turbine". Int. J. Energy Res., 1998; 22: pp. 953-964.

[44] "ANSYS-CFX Solver Theory Guide Manual". Release 11.0, 2006

[45] Launder, B. E., and Spalding, D. B., "The Numerical Computation of Turbulent Flows". Comput. Methods Appl. Mech. Eng., 1974; (3): pp. 269-289.

[46] Lui, Z., Hyun, B. S., and Hong K. Y., "Application of Numerical Wave Tank to OWC Air Chamber for Wave Energy Conversion". In: Proceedings of the 18th International Offshore and Polar Engineering Conference. Vancouver, BC, Canada, 2008.

[47] Lais, S., Liang, Q., Henggeler, U., Weiss, T., Escalar, X., and Egusquiza, E., "Dynamic Analysis of Francis Runners-Experiment and Numerical Simulation". Int. J. Fluid Machinery and Systems., 2009; (2): pp. 303-314.

[48] CFD Online., "Finite Volume". Online, http://www.cfd-online.com/Wiki/Finite_volume, 2010.